Journal of Nanomaterials

Sustainable Synthesis of Nanomaterials for Environmental Remediation and Biomedical Applications: A Way Towards Circular Economy

Lead Guest Editor: Jagpreet Singh
Guest Editors: Luminita Andronic and Valeria De Matteis

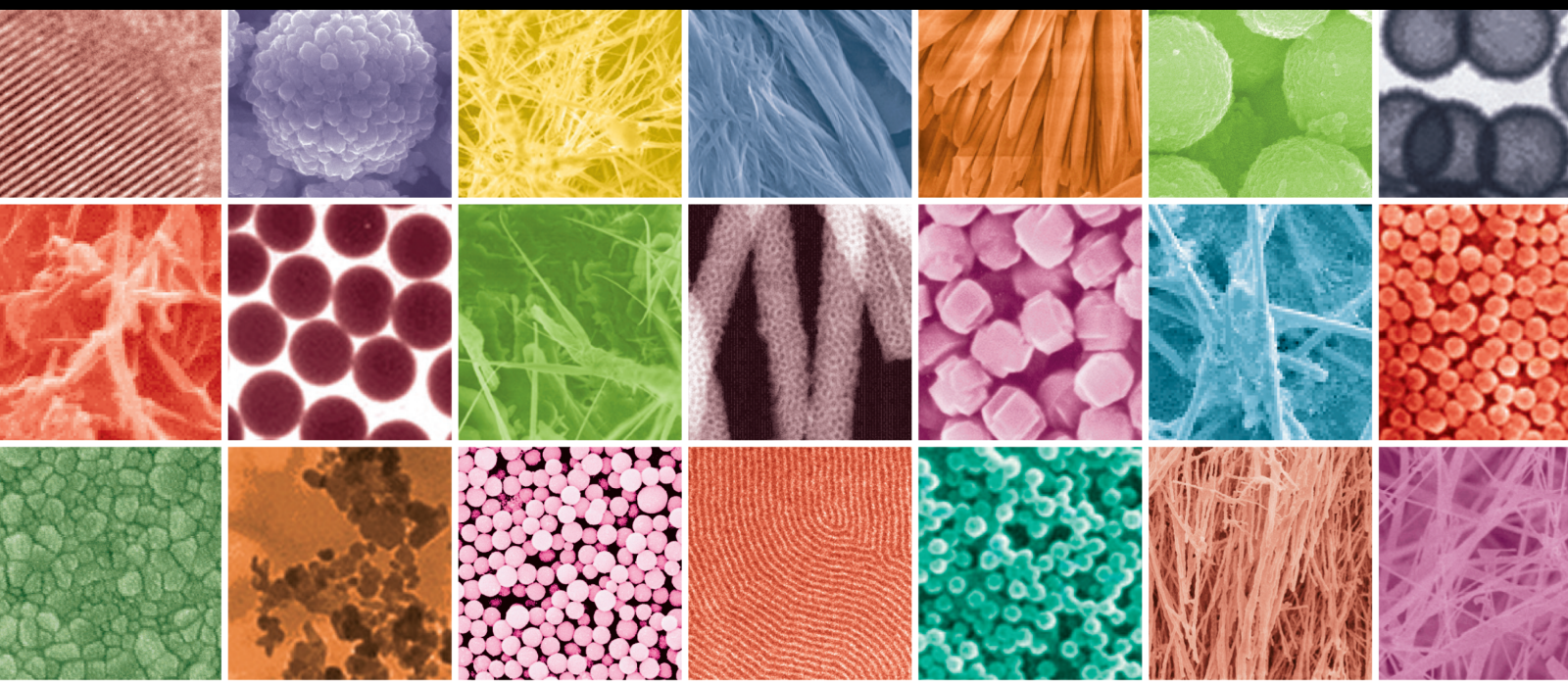

Sustainable Synthesis of Nanomaterials for Environmental Remediation and Biomedical Applications: A Way Towards Circular Economy

Journal of Nanomaterials

Sustainable Synthesis of Nanomaterials for Environmental Remediation and Biomedical Applications: A Way Towards Circular Economy

Lead Guest Editor: Jagpreet Singh
Guest Editors: Luminita Andronic and Valeria De Matteis

Contents

Hindawi
Journal of Nanomaterials
Volume 2023, Article ID 8825762, 10 pages
https://doi.org/10.1155/2023/8825762

Research Article

ZnO Nanoparticles Synthesized using Aerial Extract of *Ranunculus multifidus* Plant: Antibacterial and Antioxidant Activity

Terfo Yilma,[1] **Mikyas Kassaw**,[1] **H. C. Ananda Murthy**,[1,2] **and Aman Dekebo**[1,3]

[1]*Department of Applied Chemistry, School of Applied Natural Science, Adama Science and Technology University, Adama P.O. Box 1888, Ethiopia*
[2]*Department of Prosthodontics, Saveetha Dental College and Hospital, Saveetha Institute of Medical and Technical Science (SIMATS), Saveetha University, Chennai 600077, Tamil Nadu, India*
[3]*Institute of Pharmaceutical Sciences, Adama Science and Technology University, Adama P.O. Box 1888, Ethiopia*

Correspondence should be addressed to H. C. Ananda Murthy; anandkps350@gmail.com and Aman Dekebo; amandekeb@gmail.com

Received 28 December 2022; Revised 8 February 2023; Accepted 25 April 2023; Published 21 May 2023

Academic Editor: Jagpreet Singh

The present work reports the synthesis of zinc oxide nanoparticles (ZnO NPs) by applying an aqueous aerial extract of *Ranunculus multifidus* plant. The thermogravimetric analysis revealed that the prepared ZnO NPs are stable from 480 to 800°C. The diffraction study confirmed the hexagonal wurtzite structure for the synthesized ZnO NPs with the typical crystallite sizes of 47.92, 22.70, and 15.35 nm the volume ratios (extract to precursor) of 1 : 1, 3 : 2, and 2 : 3, respectively. The experimentally deduced E_g values are 1.82, 3.1, and 2.57 eV for 1 : 1, 3 : 2, and 2 : 3 ZnO NPs, respectively. The spherical and rod-like morphologies were confirmed for the NPs by the images taken using electron microscopy. The reducing agents in the aqueous extracts of *R. multifidus* converted the ionic zinc to zinc nanoparticles, and these NPs exhibit credible antibacterial effects against tested bacterial species. The biosynthesized ZnO NPs revealed significant antibacterial activity against *Bacillus subtilis*, *Escherichia coli*, *Pseudomonas aeruginosa*, and *Staphylococcus aureus*. The order of the antibacterial potential of the NPs was found to follow the order: *S. aureus* (17.10 ± 0.45 mm) > *B. subtilis* (16.10 ± 0.15 mm) > *E. coli* (14.5 ± 0.32 mm) > *P. aeruginosa* (13 ± 0.0 mm). The antioxidant activities of the produced ZnO NPs in various ratios showed the potentiality of phytochemicals to scavenge the free radicals, which is encouraging for the discovery of novel compounds for the treatment of cancer diseases.

1. Introduction

The novel method of plant-mediated synthesis of nanoparticles (NPs) has numerous applications in medicine, pharmacy, industry, and agriculture. Due to their toxicity, conventionally produced NPs are only occasionally used in the therapeutic setting. We are currently observing the growth and development of a new interdisciplinary scientific discipline called nanoscience [1–8]. There are many methods for the production of nanoparticles, but green synthesis is one of the most popular since it is safe for the environment, nontoxic, cheap, and extremely pure. A chemical wet method was also used to prepare nanomaterial, especially with ZnO–Ag and ZnO–Au as nanocomposite materials by using the precipitate method [9]. Noble metal and metal oxide nanoparticles including silver, copper, gold, platinum, CuO, and Ag_2O were produced using many plant extracts by adopting the green methodology. But among many metal oxide NPs, zinc oxide nanoparticles (ZnO NPs) shine in the biological and pharmaceutical industries.

In recent years, different industrial sectors, such as pharmaceuticals, cosmetic, and concrete industries, have begun to use zinc oxide as some key ceramic materials instead of the microbiological, textile, and automotive industries. Due to the worrisome rise in the incidence of bacterial infectious illnesses and their resistance to most first-line antibiotic agents, antibacterial therapy has proven challenging [10].

In the twenty-first century, this poses a serious risk to human health, necessitating urgently continuing research to find agents with stronger antibacterial and broad-spectrum activities.

Therefore, finding novel drugs to treat disease and inflammations without causing significant negative impacts on patients was the current project on which all researchers were engaged. In nanoscale formulations, ZnO NPs are now being studied as potential allies of antioxidant and antibacterial medicines. The ZnO NPs have anticancer properties and are frequently used to treat a variety of skin problems [6]. Furthermore, ZnO NPs have been used as a recent preferable tool in drug delivery and sensing horizons. Traditional medicines in a different country have a long history and are mostly based on rich, though unstandardized, pharmacopeia made primarily from plants that are used by patients at home for self-administration as well as traditional healers [11]. Due to its ethnomedicinal benefits that have been reported in various locations by different herbalists and researchers, *Ranunculus multifidus*, one of the traditional medicinal plants primarily found in Africa, particularly Ethiopia, is taken into consideration in this work [12]. The bio-diversified species of flowering plant *R. multifidus*, often known as buttercup in South Africa, belongs to the *Ranunculaceae* family. With the exception of West Africa, Madagascar, and the Arabian Peninsula; it is indigenous to Sub-Saharan Africa [12]. Anti-rheumatism, intermittent fever, and rubefacient are the three traditional uses of *Ranunculus* species [13]. In a similar situation, *R. multifidus* was also traditionally used to cure several diseases. The most widely adopted traditional uses includes treatment of TB [14], infertility, blood cleansing [15], eye infection [16], shingles and sores, malaria [17], and others. This traditional use of the plant might emanate from its phytochemical components such as flavonoids, saponins, alkaloids, glycosides, terpenoids, anthocyanins, and quinones. Despite the plants having a wide range of conventional applications, there are no reports of this amazing herb being used to synthesize nanoscale materials. The main objective of the current study was to explore or search the application of *R. multifidus* plant aerial extract as a capping and reducing agent for the synthesis of ZnO NPs because it is a rich source of bioactive compounds and investigate their antibacterial and antioxidant activity in light of the significance of green nanoparticles and research gap toward the plant mentioned. The plant extract transforms ionic zinc to metal zinc oxide nanoparticles by acting as a reducing and capping agent. Therefore, the antibacterial activity of synthesized ZnO NPs was evaluated against Gram-negative and Gram-positive bacterial strains namely, *Escherichia coli*, *Pseudomonas aeruginosa*, *Staphylococcus aureus*, and *Bacillus subtilis*. In addition, the radical scavenging activities of synthesized NPs were evaluated using the DPPH methods. The result of the present work revealed that the synthesized nanoparticles exhibited significant antibacterial activities, especially on Gram-positive pathogenic strains. The radical scavenging activities of ZnO NPs are promising for the disease-associated ROS. To the best of our knowledge, this research was the first and novel work using this plant and gives a great clue for further works, especially using nanohybrid materials to enhance the potency of nanoparticles for different biomedical applications.

2. Materials and Methods

2.1. Plant Material Collection and Identification. The aerial parts of the plant *R. multifidus* were picked from Bekoji, Oromia region, Arsi zone. The authentication of the plant was done at the National Herbarium of Ethiopia, Addis Ababa University (voucher no. TY-001).

2.2. Preparation of Plant Extracts (Broth Solution). R. multifidus fresh plant material was collected, completely cleaned with distilled and tap water to get rid of the dust, and then dried in the shade to get rid of any remaining moisture. The powdered plant materials were sieved using 180 m size sieves after being pounded into powder. The sample's aqueous extracts were made by boiling 50 g of finely ground powder for 60 min at 80°C with constant stirring. After filtering the extract using Whatman no. 1 filter paper and allowing it to cool to room temperature, the extract was kept in a refrigerator at 4°C for future experimental usage [5].

2.3. Synthesis of ZnO NPs. Three different ratios *R. multifidus* plant extract and precursor salts were used: 1 : 1, 3 : 2, and 2 : 3, 50 mL, 60 mL, 40 mL of extract and 50 mL, 40 mL, and 60 mL of 0.2 M zinc acetate ($Zn(O_2CCH_3)_2(H_2O)_2$), were mixed with 50 mL of 0.2 M NaOH, respectively.

A yellow precipitate formed after the three solutions were continuously for 2 hr at 800 rpm using a magnetic stirrer [18]. The precipitate was periodically cleaned in ethanol and distilled water to get rid of any impurities left behind, and they were then oven dried at 100°C for an hour. Using a blender, the produced dried light yellow color powder was prepared for further characterization and applications. The overall synthesis process was depicted in Figure 1.

2.4. Characterization of Biosynthesized ZnO NPs. A simultaneous DTA-TGA (DTG-60H, Shimadzu Co., Japan) study was used to examine the thermal stability and decomposition followed by the weight loss of the prepared ZnO NPs measured at the heating rate of 10°C/min. An ultraviolet–visible (UV–vis) spectrophotometer was utilized to identify the surface plasmon resonance (SPR) peak. Using Fourier transform infrared spectroscopy, the potential phytochemicals causing the reduction of metal salts into ZnO NPs were examined (FTIR). The external morphology, surface features, and elemental compositions of ZnO NPs were analyzed using -microscopic methods combined with energy-dispersive X-ray analysis (SEM-EDX).

2.5. Antibacterial Investigation of Synthesized ZnO NPs. The antibacterial activity of biosynthesized ZnO NPs was performed using the agar disc diffusion method against human infectious, *B. subtilis*, *E. coli*, *P. aeruginosa*, *and S. aureus*, bacterial strains which were American Type Culture Collection (ATCC). In nutrient broth, cultures of the test organism were grown to the late logarithmic phase. Aliquots of 100 μL from the cultures were spread on solidified nutrient agar plates. The plates were coated with the 100 μL solution of 50, 75, and 100 μg/mL concentration of ZnO NPs solution impregnated disc (6 mm). The plates were then placed upside down in the incubator at 37°C for 24 hr. To ensure that bacterial cells and agar were mixed equally, the plates were gently shaken. After

Figure 1: A schematic of the synthesis of ZnO NPs using *Ranunculus multifidus* plant extract.

the incubation period got over, different levels of zonation formed around the disc were measured using a caliper. This procedure was done for all ratios of biosynthesized ZnO NPs against standard bacterial strains.

2.6. DPPH Radical Scavenging Assay. DPPH radical scavenging assay was conducted according to the previously described standards with little modification, the DPPH test was used to evaluate the free radical scavenging activity (RSA) of the plant extract and synthesized ZnO NPs of various ratios (1 : 1, 2 : 3, and 3 : 2) salt to plant aqueous aerial extract [19]. The 1,1-diphenyl-2-picryl hydrazyl (DPPH), a persistent free radical, can decolorize in the presence of antioxidants, which is the basis for the DPPH antioxidant assay. The odd electron in the DPPH radicals is what causes the absorbance at 517 nm as well as the apparent to deep purple color. A decrease in the absorbance of the reaction mixture indicates significant free radical scavenging activity of the extract or synthesized NPs. The data were compared with those obtained with the reference ascorbic acid. In the process, the synthesized ZnO NPs of different ratios (1 : 1, 2 : 3 and 3 : 2) salt to plant extract ration were dissolved in methanol to afford 1 mg/mL. It was serially diluted in methanol to yield a 500, 250, 125, and 62.5 μg/mL concentration. Four milliliters of DPPH (0.004% DPPH in MeOH) was added to 1 mL of each concentration to make 100, 50, 25, and 12 μg/mL. Then all the samples prepared were incubated in an oven at 37°C for 30 min and then absorbance was recorded at 517 nm using a UV–vis spectrophotometer. A reaction solution without DPPH was used as blank and DPPH solution as a control. Ascorbic acid was used as standard. The percentage inhibition was calculated using the Equation (1):

$$\text{Inhibition } (\%) = \frac{\text{A control} - \text{A test}}{\text{A control}} \times 100. \quad (1)$$

The IC_{50}, or the concentration of the test substance needed to cause a 50% reduction in absorbance from that of the control solution, is another way to express the sample's ability to scavenge DPPH radicals [20]. The concentration vs. RSA% graph was produced using Excel, and the IC_{50} values were calculated from it and interpreted as the smallest IC_{50} values mean the strongest radical scavenging concentration of extracts.

3. Results and Discussion

3.1. Synthesis ZNO NPs. Using *R. multifidus* and zinc acetate dihydrate salt as a precursor, ZnO NPs were synthesized. The aerial extract from *R. multifidus* was used as a reducing and capping agent. The presence of flavonoids, phenolic compounds, tannins, saponins, anthraquinone glycosides, reducing sugars, phytosterols, steroids, terpenoids, and glycosides in the plant extracts revealed the phytochemical screening of the extracts. The information on the phytochemicals in the extract is provided in Table 1. The three main processes that go into making NPs, metal ion reduction, cluster formation, and nanoparticle development, are thought to be extremely important. The tautomeric conversion of polyphenols from

Table 1: The result of the phytochemical screening of the aerial extract of the *R. multifidus* plant.

No.	Phytochemicals	Test types/reagent	Result
1	Flavonoids	Shinoda Test	+
2	Saponins	Foam test	+
3	Phenol	Ferric chloride test	+
4	Cardiac glycosides	Keller–Killiani Test	+
5	Terpenoids	Salkowski Test	+
6	Reducing sugars	Fehling's test	–
7	Phytosterols	Salkowski Test	+
8	Tannins	Alkaline test	–
9	Anthraquinone glycosides	Borntrager's Test	+
10	Steroids	–	+
11	Alkaloids	Wagner's test	–

NB: + indicates the presence and – indicates the absence.

their enol form to their keto form can be expected to reduce the zinc ions to zinc NPs.

Additionally, the enzymes in the aerial extract of the plant assist the metal ions to create an enzyme–substrate complex, which results in the production of zinc with a protein cap [21], and it is known that the phenolic chemicals serve as ligands, bind to metal ions, decrease, and cap those ions to create nanoparticles. A prior study had also claimed that these ligands also function as regulators of particle size [21, 22]. The great propensity of phenolic compounds to chelate metals is the main cause of their antioxidant function. The hydroxyl and carboxylic groups found in phenolic compounds have a very high propensity to attract metal ions. In solution, the phenolic chemicals interact with metal ions, assisting in the nucleation and production of ZnO NPs.

3.2. Characterization of Synthesized ZnO NPs. The synthesized ZnO NPs were characterized by using the TGA and its derivative (DTA), UV–vis-DRS, FT-IR, XRD, and SEM techniques.

3.2.1. Thermogravimetric Analysis (TGA) and Its Derivative (DTA). The sample's mass loss is shown by the TGA curve, while the process's energy gain or loss is shown by the DTA curve [5]. Figure 2 depicts the thermal analysis plots of the uncalcined ZnO NPs (1 : 1).

The three primary steps were observed from the ZnO NPs TGA curves; 6.89% of the water molecules in the first curve, in the temperature range from 20 to 250°C, reveal the dehydration of adsorbed water. In the second breakdown loss, which occurs as the temperature rises from 240 to 480°C, 10.75% of Zn $(OH)_2$ transforms into ZnO NPs. The remaining decomposition losses from 480 to 800°C are not displayed in the third stage. According to the evidence of breakdown losses, residual surfactants, or steady heat follow, ZnO NPs were found to be thermally stable from 480 to 800°C. The outcome of this investigation was consistent with earlier published research [23]. As a result, for all other manufactured ZnO NPs throughout this experiment, calcination temperatures of up to 480°C were used.

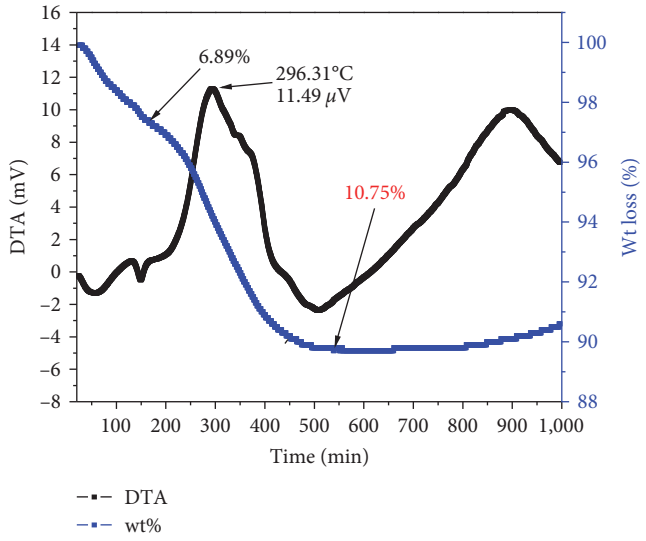

Figure 2: Thermal analysis plots of ZnO NPs obtained using the aerial extract of *Ranunculus multifidus* plant.

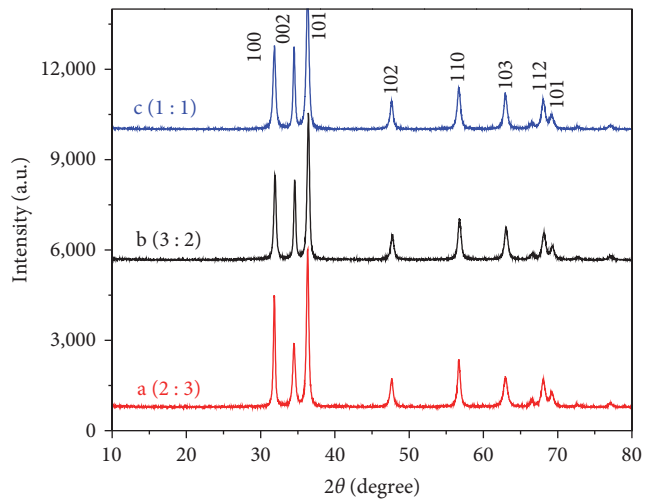

Figure 3: XRD patterns of the synthesized ZnO NPs with different ratios: (a) 2 : 3, (b) 3 : 2, and (c) 1 : 1.

3.2.2. XRD Analysis. X-ray diffraction technique was utilized to explore the structure and crystallite size of the synthesized ZnO NPs. Figure 3 displays the diffraction pattern of ZnO NPs made from zinc acetate precursor and *R. multifidus* plant aerial extract in three different volume ratios, such as (1 : 1), (2 : 3), and (3 : 2). The lattice planes (100), (002), (101), (102), (110), (103), and (112) are successively represented by the 2θ values, 32.01°, 34.50°, 36.25°, 47.71°, 56.71°, and 68.00° in the XRD analysis of ZnO NPs. All the diffraction peaks recorded for the NPs were discovered to be in compliance with the literature report [5, 23]. The findings support the synthesis of pure ZnO NPs without the creation of any secondary phase and are in good accord with Miller index values and the hexagonal wurtzite structure of ZnO (JCPDS card no. 036-145). The evaluation using Scherer's formula (Equation (2)) revealed the typical crystallite size of 47.92,

Table 2: The parameters obtained from the diffraction studies for the ZnO NPs synthesized using 1 : 1, 3 : 2, and 2 : 3 rations of the salt to extract.

Ratios of ZnO NPs	2θ (degree)	FWHM (θ)	FWHM (3.14/180)	hkl	D	D_{av} (nm)
	33.3608	0.17470	0.003049	100	49.5813	
1 : 1	35.8293	0.18160	0.00317	102	48.01849	47.92
	54.2561	0.20190	0.003524	101	46.1763	
	36.8235	0.48210	0.008424	100	18.1394	
3 : 2	15.9989	0.27670	0.004929	102	30.2815	22.70
	65.1727	0.50000	0.008727	101	19.6951	
	36.8697	0.58190	0.010156	100	15.0304	
2 : 3	65.2310	0.63670	0.011113	102	15.4716	15.35
	59.3379	0.61330	0.010704	101	15.57032	

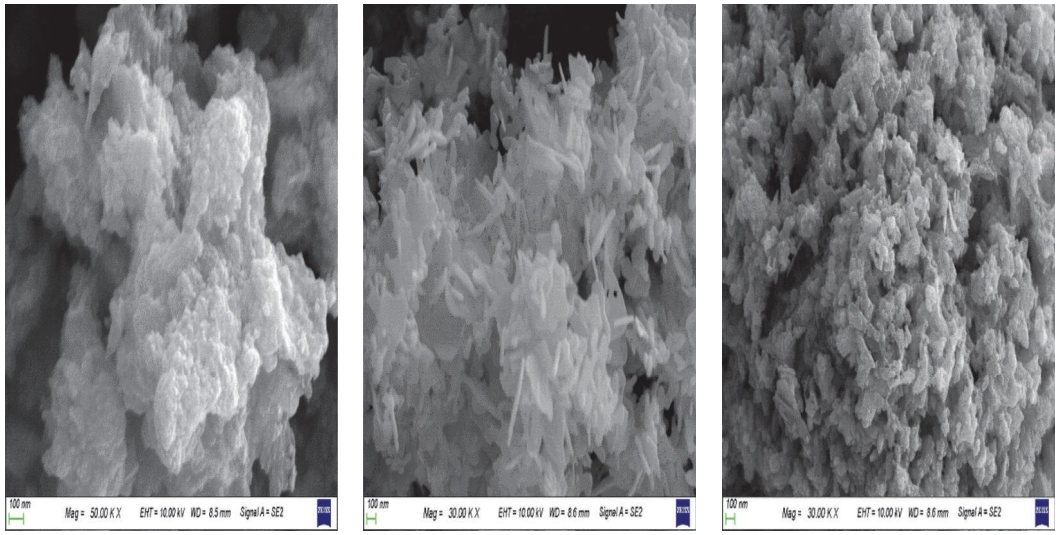

(a) (b) (c)

Figure 4: SEM images of (a) 1 : 1 ZnO, (b) 3 : 2 ZnO, and (c) 2 : 3 ZnO NPs.

22.70, and 15.35 nm for ZnO NPs prepared in the volume ratios of (1 : 1), (3 : 2), and (2 : 3), respectively.

$$D = \frac{K}{B \cos \theta}, \tag{2}$$

where D is the crystallite size, K is 0.9 diffraction constant (shape factor), λ is 1.54 (X-ray source wavelength), β is the full width at half maximum intensity (FWHM) in radians, and θ is the angle of diffraction.

Table 2 displays the estimated and measured XRD parameters for crystallite size. The calculated and measured crystallite size XRD characteristics are shown in Table 2. The results revealed that the ratio of the plant extract grew from 1 : 1 (47.92 nm) to 3 : 2 (22.7 nm) and to 2 : 3 (15.35 nm) volume ratios, the average crystal size of ZnO NPs were found to increase. Since a greater amount of the plant extract was used during the synthesis process, it results in effective capping and stabilization of the synthesized nanoparticles and hinders the process of aggregation. This precisely matches the previously stated method of the production of ZnO NPs [24].

3.2.3. SEM Analysis. SEM was used to examine the surface morphological characteristics of the ZnO NPs. The micrographs are presented in Figure 4(a)–4(c). Figure 4(a) displays a micrograph of ZnO NPs produced using a 1 : 1 volume ratio of plant aerial extract and zinc acetate salt. ZnO NPs with a 1 : 1 volume ratio appeared as a honeycomb-like structure in the SEM picture. The increase of the nanoparticles' size and the accumulation of zinc acetate and plant extract on their surface are what caused it to occur. Due to the increased concentration of zinc ions followed by aggregation on the surface for ZnO NPs in 3 : 2 volume ratios resulted in a road-like form and the ZnO NPs with 2 : 3 volume ratio, exhibited a spherical form [25]. According to the current work and earlier literature findings, the ability of the extract to serve as a cap during the nucleation, aggregation, and formation of NPs was what caused the reduction in size upon increasing plant extract concentration [25].

3.2.4. Fourier Transform Infrared (FTIR) Analysis. Figure 5 shows the FTIR spectra of ZnO NPs and aerial extract of *R. multifidus* plant. Biomolecules were found in the extract and NPs by FTIR spectral analysis. The major peaks that were

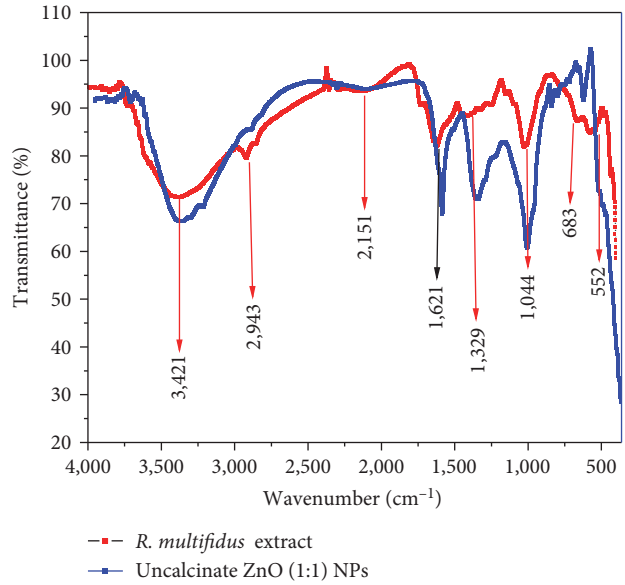

Figure 5: FTIR spectra of *Ranunculus multifidus* plant extract and synthesized ZnO NPs (1 : 1).

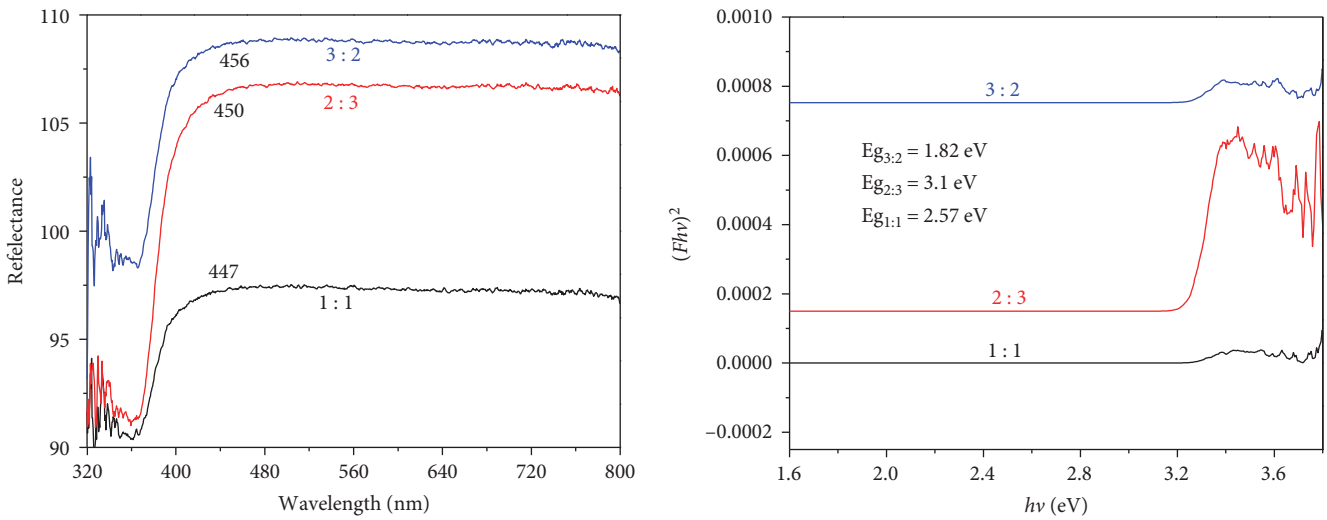

Figure 6: (a) UV–visible reflectance spectra, and (b) band gap energy of ZnO NPs.

detected at 3,421 and 2,943 cm^{-1} represent, sp^3 C–H stretching vibrations and the OH stretching vibration of carboxylic acid, respectively. The vibration of the CN moiety from the protein molecule of the extract is responsible for the peak at 2,151 cm^{-1}. The peak at 1,621 cm^{-1} is related to carbonyl groups that have undergone C=O stretching and may be acidic carbonyl groups. Sharp peaks around 1,329 cm^{-1} indicate the existence of the carboxylic acid COO– group. Additionally, it was demonstrated that the amine and carboxylate groups in the *R. multifidus* aerial extract were in charge of adhering to the surface of ZnO and stabilizing the biosynthesized ZnO NPs as well as fitting the prior literature study [21]. Around 1,044 cm^{-1}, the C–O–C stretching becomes visible. The peak at around 552 cm^{-1} can be attributed to the stretching vibration of the Zn–O bond. The bending vibrations of Zn–O–H bonds resulted in a tiny peak at 683 cm^{-1}.

3.2.5. UV–Vis–DRS Spectral Analysis. Diffuse reflectance spectroscopy (DRS) was used to assess the optical energy band gap (E_g) values of the synthesized ZnO NPs in volume ratios (1 : 1, 2 : 3, and 3 : 2) as shown in Figure 6. The sample's reflectance spectrum was found to be highly reflective between 447 and 456 nm in the UV spectrum, attaining a practically constant value thereafter, and the results were consistent with the report [26, 27]. The Kubelka–Munk formula (Equation (3)) was applied to convert the measured reflectance to absorbance.

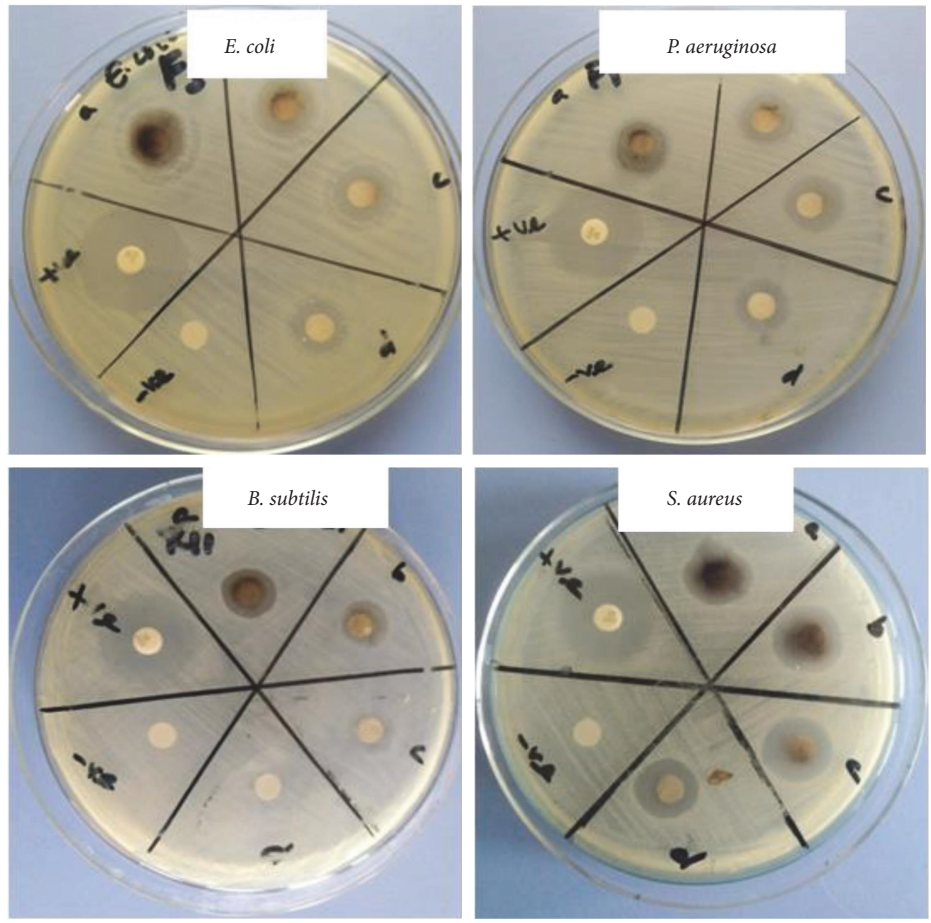

Figure 7: Inhibition zone of bacterial strain using disc diffusion methods using 2 : 3 ratio of ZnO NPs sample.

$$F(R)h\nu = A\left(h\nu - E_g\right)^n, \quad (3)$$

where A is the transition probability, $h\nu$ is photon energy and the exponent factor, n is the nature of the optical transition (n can take up the values ½ or 2).

The bandgap energies (E_g) of synthesized ZnO NPs with the volume ratios of (1 : 1), (2 : 3), and (3 : 2) were 1.82, 3.1, and 2.57 eV, respectively, and were calculated based on Equation (3); the fraction of reflectance (F), the photon energy ($h\nu$), and direct bandgap energies (E_g). ZnO (2 : 3) NPs have a higher E_g value than the other two volume ratios. On the other hand, the 2 : 3 ratio's average crystallite size from XRD shows that it is smaller than the other counterpart. As the concentration of the extract increases, the increased concentration of the phytochemicals stabilizes small particles by effectively capping them. This intern accounts for the decreased aggregation effect. If the particle size is very small, light interacts with the samples instead of being absorbed by it, with some of the light being reflected and scattered. This intern demonstrates the prior report's finding that the band gap energy of greenly produced ZnO NPs has an inverse relationship with the average crystalline size [27].

3.3. Antibacterial Activity. *S. aureus*, *B. subtilis*, *E. coli*, and *P. aeruginosa* were all tested pathogens, and the ZnO NPs have exhibited a wide spectrum of antibacterial activity against all of them. This study evaluated how biomolecules and ZnO NPs worked together to combat four pathogenic diseases. Three concentrations of Co-clotrimazole, DMSO, and ZnO NPs (50, 75, and 100 μg/mL) were used to determine the zone of inhibition. The structural differences in bacteria cell walls are assumed to be the reason why ZnO NPs were discovered to have superior antibacterial action against Gram-positive bacteria than Gram-negative bacteria [5, 21]. The outer lipopolysaccharide membrane of Gram-negative bacteria, which renders the cell wall resistant to antibacterial chemical substances, is the source of these variances in morphological constitutions between these micro-organisms. Gram-positive bacteria, on the other hand, are more prone to permeability barriers since they only have an exterior peptidoglycan layer. Due to their more intricate cell walls than Gram-positive bacteria, Gram-negative bacteria are less susceptible to antibacterial medications and act as a diffusion barrier. The presence of bioactive chemicals that functions as capping and stabilizing agents on the surface of NPs can be partially blamed for the antibacterial activities of NPs. The ZnO NPs exhibited excellent antibacterial activity against both Gram-positive (*S. aureus* and *B. subtilus*) and Gram-negative (*E. coli* and *P. aeruginosa*) bacterial strains, as shown in Figure 7 (Table 3). When we compared the inhibition zone for each

Table 3: Zone of inhibition (mm) of ZnO nanoparticles against Gram positive and Gram-negative bacterial strains.

Ratios	Conc. (μg/mL)	Bacteria species and zone of inhibitions in mm			
		E. coli ATCC 25922	*S. aureus* ATCC25923	*P. aeruginosa* ATCC27853	*B. subtilis* ATCC6633
1 : 1 ZnO	a 50	6 ± 1.12	7.5 ± 0.56	5.5 ± 0.32	8.24 ± 0.30
	b 75	7.8 ± 0.76	9.8 ± 0.48	6.32 ± 0.25	9.5 ± 0.73
	c 100	10.7 ± 0.45	13.85 ± 0.44	9.3 ± 0.78	12.9 ± 0.18
2 : 3 ZnO	a 50	10 ± 0.67	12.7 ± 0.25	9.2 ± 0.36	12 ± 0.54
	b 75	12.8 ± 0.40	14.9 ± 0.65	11.7 ± 0.65	14 ± 0.50
	c 100	14.5 ± 0.32	17.10 ± 0.45	13 ± 0.0	16.10 ± 0.15
3 : 2 ZnO	a 50	8 ± 0.00	10 ± 0.52	8.2 ± 0.41	9 ± 0.74
	b 75	11 ± 0.50	11.5 ± 0.32	9.0 ± 0.55	11.34 ± 0.5
	c 100	$13.72.10 \pm 0.24$	14 ± 0.65	12.45 ± 0.82	14.53 ± 0.32
Standard	Co-clotrimazole	22.5 ± 0.27	25 ± 0.55	22 ± 0.42	24 ± 0.15

Table 4: % radical scavenging activity of the ZnO NPs.

Conc. (μg/mL)	Absorbance of sample				DPPH (%) inhibition			
	P_1M_1	P_2M_3	P_3M_2	AA	P_1M_1	P_2M_3	P_3M_2	AA
12.5	0.47	0.36	0.25	0.02	48.85	60.82	72.80	98.44
25	0.42	0.31	0.21	0.01	54.23	66.26	77.14	98.5
50	0.38	0.28	0.18	0.013	58.64	69.53	80.41	98.54
100	0.32	0.25	0.15	0.012	65.18	72.79	83.67	98.59
Control 0.9188								

P, plants extracts, *M*, metal ions; AA, ascorbic acid; the number stands for volume of ratios.

ratio of biosynthesized NPs, the maximum inhibition was seen for (2 : 3) ZnO NPs for each strain. This could be a result of the synergistic effects of phytochemicals included in plant extracts as well as the propensity of functional groups like phenolics and amines to interact with metal surfaces and disturb membrane integrity. At a sample concentration of 100 μg/mL, the inhibition zone for each strain is displayed in descending order for this maximum ratio; *S. aureus* (17.10 ± 0.45 mm), *B. subtilus* (16.10 ± 0.15 mm), *E. coli* (14.5 ± 0.32 mm), *P. aeruginosa* (13 ± 0.0 mm); the NPs with a 1 : 1 ratio showed lesser inhibition [24]. The alternative explanation could be that Zn antimicrobial activities are owing to its toxicity, which was noted in this experimental study and other similar works that have previously reported on the antimicrobial properties of this metal-based NPs [24, 28].

The inhibition zone of each strain was concentration-dependent, which is explained by the linear association between NPs concentration and the inhibitory effect, according to the table of antibacterial activity results. Scientists have proposed a few potential bactericidal pathways in response to ZnO NPs' interactions with bacteria. Some researchers asserted that because smaller NPs have more surface reactivity, the released Zn^{2+} ions can penetrate them more deeply. One of the most popular theories for an antibacterial mechanism involves the release of Zn^{2+} from ZnO NPs, which is known to block several bacterial cell functions, including active transport, bacterial metabolism, and enzyme activity. Because of the toxicity properties of Zn^{2+}, this ultimately causes bacteria to perish [28–32].

Some other researchers made the hypothesis that the production of reactive oxygen species (ROS), which results in oxidative stress and, ultimately, cell damage or death, is what triggers antibacterial action. ZnO NPs frequently use the generation of ROS as an antibacterial strategy [5, 24]. The attachment of NPs to the bacterial cell membrane by electrostatic forces is another potential mechanism for the antibacterial activity of ZnO NPs. This interaction could harm the bacterial cell's integrity and alter the membrane plasma structure, allowing internal contents to seep out and ultimately leading to cell death [8, 21].

3.4. DPPH Radical Scavenging Assay. The synthesized ZnO NPs demonstrated the presence of antioxidant capabilities in an *in vitro* antioxidant experiment. The relationship between different volume ratios of synthetic ZnO NPs produced from aerial extracts and their capacity to scavenge DPPH radicals was proven (Table 4). All the antioxidant models showed a percentage of inhibitions, indicating that the produced ZnO NPs were effective at scavenging free radicals up to the specific concentration (Figure 8). According to the results in Table 4, the synthesized NPs have a negligible antioxidant effect in comparison to the reference standard.

P_3M_2 had the highest level of radical inhibition values of 83.67% at maximum concentration (100 μg/mL), which was comparable to L-ascorbic acid at this concentration when comparing the radical scavenging capability of various ratios. The P_2M_3 test yielded results that were second-most promising, with antiradical inhibition effects (100 μg/mL) of

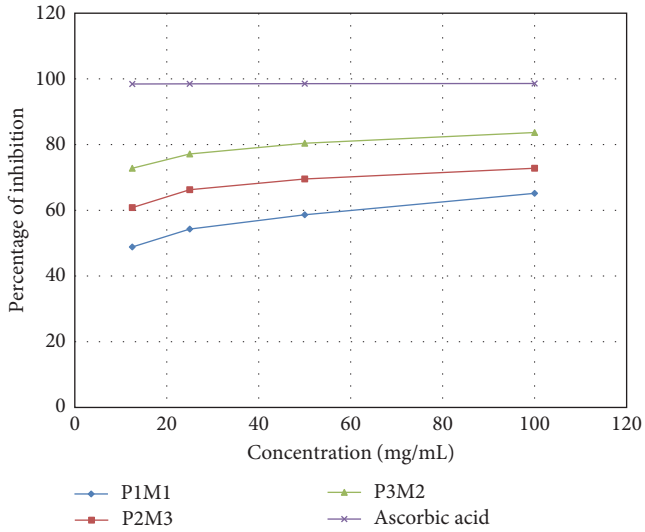

FIGURE 8: Graphical representation of radical scavenging power of synthesized ZnO NPs using different volume ratios of plant extracts to metal.

72.79% compared with L-ascorbic acid, which inhibited at a rate of 98.59% at the same concentration (Table 4). Overall, the results demonstrate that the synthetic zinc oxide nanoparticles generated from *R. multifidus* aerial extracts offer a useful lead for future research into the development of antioxidant drugs to treat various cardiovascular diseases using more sophisticated instrumentation and cutting-edge technology. To compare the present result with previously reported work, zinc oxide-silver (ZnO–Ag) and zinc oxide-gold (ZnO–Au) nanocomposites were prepared through wet chemical process and laced into single-walled carbon nanotubes (SWCNTs) to yield ZnO–Ag-SWCNTs and ZnO–Au-SWCNTs hybrids, which shows significant phagocytic and bactericidal activities against the Gram-negative bacteria *E. coli* and Gram-positive *S. aureus* which support the current antibacterial effect of ZnO NPs using plant extracts [33].

4. Conclusion

Synthesis of ZnO NPs from aqueous extracts of aerial parts of *R. multifidus* using green methods was confirmed by the formation of yellow precipitates. The synthesized NPs were characterized by using XRD, SEM, TGA-DTA, FTIR, and UV-DRS, and the result is consistent with previously reported articles for ZnO NPs. FTIR result shows the nitro compounds and aromatic amines as reducing and capping agents, while analysis of produced ZnO nanoparticles revealed a UV–vis absorption peak at 442 nm. XRD examination demonstrated that every diffraction peak matched the hexagonal wurtzite structure of ZnO NPs. ZnO NPs' spherical shape was confirmed by image taken using scanning electron microscopy. The synthesized ZnO NPs revealed a significant antibacterial activity against *E. coli*, *P. aeruginosa*, *S. aureus*, and *B. subtilis* relatively in all ratios. The significant phagocytic and bactericidal activities observed against the Gram-negative bacteria *E. coli* and Gram-positive *S. aureus* support the current antibacterial effect of ZnO NPs. The antiradical activities of produced ZnO NPs in various ratios show that plant material has the ability to scavenge free radicals. Generally, the present work indicates that there is a promising antibacterial and antioxidant nanoscale pharmaceutical product from *R. multifidus* aqueous aerial extracts using zinc metal and we strongly recommend testing more antifungal and anticancer activities of synthesized ZnO NPs in the future.

Data Availability

The data used to support the findings of this study are included within this article.

Conflicts of Interest

The authors declare that they have no conflicts of interest.

Acknowledgments

The authors are grateful to Adama Science and Technology University for the support rendered towards this work. We are also grateful to the World Academy of Sciences (TWAS) and the United Nations Educational, Scientific and Cultural Organization (UNESCO) for financing this research with funds allocated to the AD research team under the TWAS Research Grant RGA No. 20-274 RG/CHE/AF/AC_G – FR3240314163.

References

[1] M. O. Akpotu, P. M. Eze, C. C. Abba, C. U. Nwachukwu, F. B. C. Okoye, and C. O. Esimone, "Metabolites of endophytic fungi isolated from *Euphorbia hirta* growing in Southern Nigeria," *Chemical Science Review and Letters*, vol. 6, no. 21, pp. 12–19, 2017.

[2] A. B. Muluye, A. G. Desta, S. K. Abate, and G. T. Dano, "Antimalarial activity of the root extract of *Euphorbia abyssinica* (*Euphorbiaceae*) against *Plasmodium berghei* infection in mice," *Malaria Journal*, vol. 18, Article ID 261, 2019.

[3] F. Kaaniche, A. Hamed, A. S. Abdel-Razek et al., "Bioactive secondary metabolites from new endophytic fungus *Curvularia*. sp isolated from *Rauwolfia macrophylla*," *PLOS ONE*, vol. 14, no. 6, Article ID e0217627, 2019.

[4] B. Abebe, H. C. A. Murthy, and Y. Dessie, "Synthesis and characterization of Ti–Fe oxide nanomaterials: adsorption–degradation of methyl orange dye," *Arabian Journal for Science and Engineering*, vol. 45, pp. 4609–4620, 2020.

[5] M. G. Demissie, F. K. Sabir, G. D. Edossa, and B. A. Gonfa, "Synthesis of zinc oxide nanoparticles using leaf extract of *Lippia adoensis* (Koseret) and evaluation of its antibacterial activity," *Journal of Chemistry*, vol. 2020, Article ID 7459042, 9 pages, 2020.

[6] H. Jan, M. Shah, A. Andleeb et al., "Plant-based synthesis of zinc oxide nanoparticles (ZnO-NPs) using aqueous leaf extract of *Aquilegia pubiflora*: their antiproliferative activity against HepG2 cells inducing reactive oxygen species and other *in vitro* properties," *Oxidative Medicine and Cellular Longevity*, vol. 2021, Article ID 4786227, 14 pages, 2021.

[7] M. Naseer, U. Aslam, B. Khalid, and B. Chen, "Green route to synthesize zinc oxide nanoparticles using leaf extracts of *Cassia fistula* and *Melia azadarach* and their antibacterial potential," *Scientific Reports*, vol. 10, Article ID 9055, 2020.

[8] A. Raj and R. Lawerence, "Green synthesis and characterization of ZnO nanoparticles from leafs extracts of *Rosa indica* and its antibacterial activity," *RASĀYAN Journal of Chemistry*, vol. 11, no. 3, pp. 1339–1348, 2018.

[9] M. K. A. Mohammed, Z. J. Taqi, A. M. A. Hassen, M. S. Jabir, and D. S. Ahmed, "SWCNTs/ZnO-Ag/ZnO-Au nanocomposite increases bactericidal activity of phagocytic cells against *Staphylococcus aureus*," *AIP Conference Proceedings*, vol. 2372, no. 1, Article ID 020001, 2021.

[10] D. Zeleke, R. Eswaramoorthy, Z. Belay, and Y. Melaku, "Synthesis and antibacterial, antioxidant, and molecular docking analysis of some novel quinoline derivatives," *Journal of Chemistry*, vol. 2020, Article ID 1324096, 16 pages, 2020.

[11] W. Abebe, "An overview of ethiopian traditional medicinal plants used for cancer treatment," *European Journal of Medicinal Plants*, vol. 14, no. 4, pp. 1–16, 2016.

[12] M. Z. Bhatti, A. Ali, A. Ahmad, A. Saeed, and S. A. Malik, "Antioxidant and phytochemical analysis of *Ranunculus arvensis* L. extracts," *BMC Research Notes*, vol. 8, Article ID 279, 2015.

[13] M. S. Aslam, B. A. Choudhary, M. Uzair, and A. S. Ijaz, "The genus *Ranunculus*: a phytochemical and ethnopharmacological review," *International Journal of Pharmacy and Pharmaceutical Sciences*, vol. 4, no. 5, pp. 15–22, 2012.

[14] B. Madikizela, L. Kambizi, and L. J. McGaw, "An ethnobotanical survey of plants used traditionally to treat tuberculosis in the eastern region of O.R. Tambo district, South Africa," *South African Journal of Botany*, vol. 109, pp. 231–236, 2017.

[15] H. de Wet and S. C. Ngubane, "Traditional herbal remedies used by women in a rural community in northern Maputaland (South Africa) for the treatment of gynaecology and obstetric complaints," *South African Journal of Botany*, vol. 94, pp. 129–139, 2014.

[16] M. Giday, Z. Asfaw, Z. Woldu, and T. Teklehaymanot, "Medicinal plant knowledge of the bench ethnic group of Ethiopia: an ethnobotanical investigation," *Journal of Ethnobiology and Ethnomedicine*, vol. 5, Article ID 34, 2009.

[17] B. Sirak, L. Mann, A. Richter, K. Asres, and P. Imming, "In vivo antimalarial activity of leaf extracts and a major compound isolated from *Ranunculus multifidus* forsk," *Molecules*, vol. 26, no. 20, Article ID 6179, 2021.

[18] R. S. Devi and R. Gayathri, "Green synthesis of zinc oxide nanoparticles by using hibiscus rosa-sinensis," *International Journal of Current Engineering and Technology*, vol. 4, no. 4, pp. 2444–2446, 2014.

[19] K. Dulta, G. K. Ağçeli, P. Chauhan, R. Jasrotia, and P. K. Chauhan, "Ecofriendly synthesis of zinc oxide nanoparticles by *Carica papaya* leaf extract and their applications," *Journal of Cluster Science*, vol. 33, pp. 603–617, 2022.

[20] A. Kalbessa, A. Dekebo, H. Tesso, T. Abdo, N. Abdissa, and Y. Melaku, "Chemical constituents of root barks of *Gnidia involucrata* and evaluation for antibacterial and antioxidant activities," *Journal of Tropical Medicine*, vol. 2019, Article ID 8486214, 8 pages, 2019.

[21] T. Desalegn, H. C. A. Murthy, and Y. A. Adimasu, "Medicinal plant syzygium guineense (Willd.) DC leaf extract mediated green synthesis of Ag nanoparticles: investigation of their antibacterial activity," *Ethiopian Journal of Science and Sustainable Development*, vol. 8, no. 1, pp. 1–12, 2021.

[22] B. A. Lemecho, F. K. Sabir, D. M. Andoshe et al., "Biogenic synthesis of Cu-doped ZnO photocatalyst for the removal of organic dye," *Bioinorganic Chemistry and Applications*, vol. 2022, Article ID 8081494, 10 pages, 2022.

[23] A. A. Menazea, A. M. Ismail, and A. Samy, "Novel green synthesis of zinc oxide nanoparticles using orange waste and its thermal and antibacterial activity," *Journal of Inorganic and Organometallic Polymers and Materials*, vol. 31, pp. 4250–4259, 2021.

[24] E. F. El-Belely, M. M. S. Farag, H. A. Said et al., "Green synthesis of zinc oxide nanoparticles (ZnO-NPs) using *Arthrospira platensis* (class: cyanophyceae) and evaluation of their biomedical activities," *Nanomaterials*, vol. 11, no. 1, Article ID 95, 2021.

[25] M. Rafique, R. Tahir, S. S. A. Gillani et al., "Plant-mediated green synthesis of zinc oxide nanoparticles from *Syzygium Cumini* for seed germination and wastewater purification," *International Journal of Environmental Analytical Chemistry*, vol. 102, no. 1, pp. 23–38, 2022.

[26] E. T. Bekele, Y. D. Sintayehu, H. C. A. Murthy et al., "Synthesis of ZnO nanoparticles mediated by natural products of *Acanthus sennii* leaf extract for electrochemical sensing and photocatalytic applications: a comparative study of volume ratios," *Chemical Papers*, vol. 76, pp. 5967–5983, 2022.

[27] T. S. Aldeen, H. E. A. Mohamed, and M. Maaza, "ZnO nanoparticles prepared via a green synthesis approach: physical properties, photocatalytic and antibacterial activity," *Journal of Physics and Chemistry of Solids*, vol. 160, Article ID 110313, 2022.

[28] S. A. Wani, B. A. Khatoon, and F. Khanum, "Antioxidant catalytic and biological activities of zinc oxide nanoparticles synthesized by using lagerstreomia specio leaves," *International Journal of Innovations in Engineering Research and Technology*, vol. 8, no. 8, pp. 182–191, 2021.

[29] B. Abebe, E. A. Zereffa, and H. C. A. Murthy, "Synthesis of poly(vinyl alcohol)-aided ZnO/Mn_2O_3 nanocomposites for acid orange-8 dye degradation: mechanism and antibacterial activity," *ACS Omega*, vol. 6, no. 1, pp. 954–964, 2021.

[30] B. Abebe, H. C. A. Murthy, E. A. Zereffa, and Y. Adimasu, "Synthesis and characterization of ZnO/PVA nanocomposites for antibacterial and electrochemical applications," *Inorganic and Nano-Metal Chemistry*, vol. 51, no. 8, pp. 1127–1138, 2021.

[31] N. B. Raj, N. T. P. Gowda, O. S. Pooja et al., "Harnessing ZnO nanoparticles for antimicrobial and photocatalytic activities," *Journal of Photochemistry and Photobiology*, vol. 6, Article ID 100021, 2021.

[32] K. D. Dejen, E. A. Zereffa, H. C. A. Murthy, and A. Merga, "Synthesis of ZnO and ZnO/PVA nanocomposite using aqueous moringa oleifeira leaf extract template: antibacterial and electrochemical activities," *Reviews on Advanced Materials Science*, vol. 59, no. 1, pp. 464–476, 2020.

[33] O. Al Rugaie, M. S. Jabir, M. K. A. Mohammed et al., "Modification of SWCNTs with hybrid materials ZnO–Ag and ZnO–Au for enhancing bactericidal activity of phagocytic cells against *Escherichia coli* through NOX2 pathway," *Scientific Reports*, vol. 12, Article ID 17203, 2022.

Hindawi
Journal of Nanomaterials
Volume 2023, Article ID 5485632, 11 pages
https://doi.org/10.1155/2023/5485632

Research Article

Radiosensitivity Enhancement using Triptorelin Conjugated Bismuth Sulfide Nanoparticles (Bi_2S_3@BSA) in Radiotherapy for Breast Cancer Cells

Yazdan Choghazardi,[1] **Hosein Azimian**,[1] **Alireza Montazer Abadi**,[1] **Milad Mohammadi Khoshisani**,[1] **Fereshteh Vaziri Nezamdoust**,[1,2] **and Hamid Gholamhosseinian**[1]

[1]*Department of Medical Physics, Faculty of Medicine, Mashhad University of Medical Sciences, Mashhad, Iran*
[2]*Department of Applied Cell Science, Faculty of Advanced Medical Sciences, Tabriz University of Medical Sciences, Tabriz, Iran*

Correspondence should be addressed to Hamid Gholamhosseinian; gholamhosseinianh@mums.ac.ir

Received 9 November 2022; Revised 6 February 2023; Accepted 8 April 2023; Published 6 May 2023

Academic Editor: Jagpreet Singh

The aim of this study was to assess the radiosensitivity of bismuth sulfide nanoparticles conjugated with a synthetic agonist analog of gonadotropin-releasing hormones in targeted radiotherapy for breast cancer. After synthesis and characterization of nanoparticles, cytotoxicity of nanoparticles was measured by MTT assay, and the survival fraction was determined by colony formation assay. Finally, flow cytometry was performed to identify the mechanism of radiosensitization. Characterization results determined the spherical shape of Bi_2S_3@BSA with an average size of 8.649 ± 1.6 nm, and Fourier transform infrared confirmed the successful binding of triptorelin to the surface of the nanoparticles. MTT test results show that the Bi_2S_3@BSA–triptorelin did not cause any toxicity ($P < 0.05$) even up to 75 μg/ml. At all doses of ionizing radiation, colony formation assays showed that the nontoxic concentration of Bi_2S_3@BSA–triptorelin significantly increased cell death in MCF-7 cells compared to Bi_2S_3@BSA ($P < 0.05$). The apoptosis test also confirmed colony formation assay results at all doses and introduced apoptosis as a mechanism of radiosensitivity produced by nanoparticles. Certainly, targeted bismuth sulfide nanoparticles can be a good candidate for increasing radiosensitivity against tumor cells.

1. Introduction

Cancer is one of the leading causes of death in humans. Therefore, cancer treatment is currently a major challenge [1]. Common cancer treatments include surgery, radiation therapy (RT), chemotherapy, hormonal therapy, or combination therapy [2]. RT is commonly used to treat over 50% of cancer patients [3] and 80%–90% of breast cancer patients [4]. Although RT has significant advantages, it is a nonselective technic because radiation cannot distinguish between normal and cancer cells; therefore, the beam must be confined to the target volume [5]. To overcome this disadvantage, different strategies, such as tomotherapy, image-guided radiotherapy, and intensity-modulated radiotherapy, can be used to deliver the maximum dose to tumor tissue while protecting surrounding normal tissue [4, 6]. However, the equipment-based solution to increase the quality of RT may be limited because a more accurate irradiation volume can lead to excluding significant undetectable cancer cells [7]. Improves tumor response to radiation is another mechanism for enhancement of the radiotherapy ratio [8]. It is possible with a different mechanism, such as using radiosensitizer compounds [9] and molecular regulators of mRNAs (miRNA) [10]. As a definition, when used in combination with radiation, radiosensitizer compounds enhance the death of cancer cells while having a minimal effect on healthy tissue [11]. In recent years, advances in tumor therapy have been attained through methods such as enhanced cellular internalization (using nanoparticles less than 500 nm in diameter) [12]. Strategies based on nanomaterial-mediated tumor radiosensitization are mainly adopted to improve the energy deposition of ionizing radiation in the irradiated volume. This can accelerate the production of

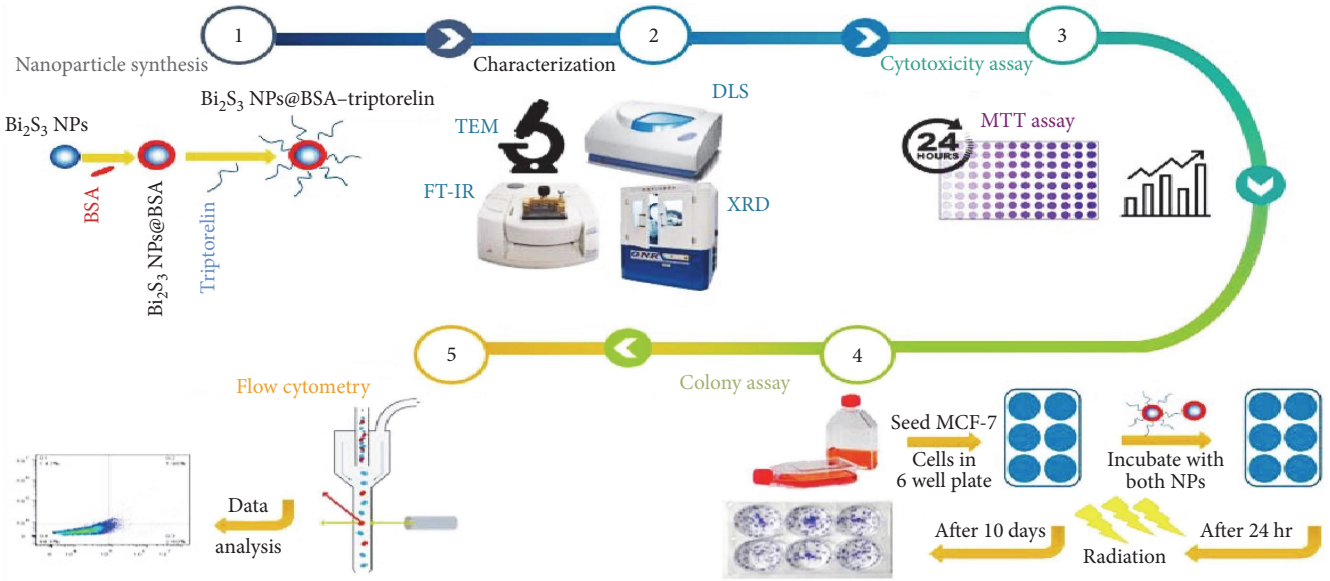

FIGURE 1: Schematic illustration of targeted Bi_2S_3@BSA NPs as a targeted radiosensitizer for radiotherapy.

reactive oxygen species to make cancer cells more sensitive to radiation [13]. Since metal nanoparticles, such as gold, platinum, and bismuth, showed radio-enhancing specifications [14]. Nanoparticles' internalization into tumor tissue could elevate localized energy deposition through free electrons and radical species. As a result, a similar degree of tumor destruction is achieved with lower radiation doses [15]. Among the high atomic number nanoparticles, bismuth (the heaviest stable nonradioactive element) is a better candidate as a radiosensitizer which improves the quality of RT compared to other nanoparticles [14] since, as one of the heaviest metal atoms, it has shown low toxicity, has a high electron density and is appropriate to absorb ionizing X-ray [16]. Another important advantage is that it is (until 2016) ~2,000 times less expensive than gold per mole [17]. In comparison to other nanoparticles (like gold), bismuth nanoparticles can better act as radiosensitizers to elevate the radiation dose delivered to tumors. This is because the number of photoelectric interactions is more [18]. Conventional drug-based radiosensitizers that do not have an efficient targeting function are most effective at the tumor site, but radiosensitivity heavily depends on the accurate localization of the radiosensitizers to cancer cells [19]. Paul Ehrlich introduced the concept of targeted drugs. This hypothesis states that tumors have specific antigens and that some factors, such as antibodies, can enhance drug delivery to tumor sites and kill them [20]. Biomolecules that bind to the surface of nanoparticles can interact with their receptors on the cell's plasma membrane. This phenomenon can be used to engineer the surface of nanoparticles with specific functional ligands (such as antibodies, proteins, or peptides) to target-specific receptors on the cell surface for medical purposes [21, 22]. Peptides are inexpensive, have higher activity per mass compared to antibodies, are more stable at room temperature, are more tissue-penetrating (to tumors or organs), and induce immune responses to antibodies [23, 24]. Peptide-conjugated metal nanoparticles have been shown to selectively attack tumor cells without affecting normal tissues [25]. Triptorelin (pGlu-His-Trp-Ser-Tyr-DTrp-Leu-Arg-Pro-Gly-NH_2) is a species of LHRH (luteinizing hormone-releasing hormone) receptor agonist whose action mechanism and affinity for binding to LHRH or GnRH (gonadotropin-releasing hormone) receptors is similar to natural LHRH [26]. Moreover, direct antiproliferative effects of the triptorelin in breast cancer cells that express GnRH receptors (such as MCF-7) have been demonstrated [27]. An ideal radiosensitizer should enhance the efficacy of RT by inducing radiosensitivity, good tumor-targeting ability, and low toxicity [19]. Herein, efforts were made to develop a novel targeted-radiosensitizer by targeting the GnRH receptors on the surface of MCF-7 cells (studies showed that the expression of these receptors and specific binding sites for LHRH analog in the membrane of MCF-7 cells had been determined) [27, 28] in order to enhance the quality and minimize the side effects of RT. In this study, we investigated the cytotoxicity, radiosensitization effects, and mechanism of radiosensitivity of targeted Bi_2S_3@BSA NPs with Triptorelin after treatment with a 6 MV photon beam in MCF-7 cell line (Figure 1).

2. Materials and Methods

2.1. Synthesis of Bi_2S_3@BSA NPs Conjugated with Triptorelin. Aqueous bismuth nitrate of 2.8 ml in 3 M HNO_3 solution at a concentration of 25 mM and a temperature of 25°C was introduced dropwise into 40 ml BSA solutions at a concentration of 66 mg/ml and a temperature of 25°C under vigorous stirring in less than 2 min. After 2 min, 6 ml NaOH solution (5 M) was added at a single instance, and the color of the solution began to change from pale yellow to light brown and then to dark black in 10 min. All synthesis steps were performed at room temperature. After 12 hr aging,

the resulting compound was centrifuged at 12,000 rpm for 15 min. Finally, in order to purify synthesized nanoparticles, they were dialyzed for 48 hr against Milli-*Q* water to eliminate any possible debris. To conjugate Bi_2S_3@BSA with triptorelin, 1 ml of the synthesized nanoparticles was placed on a magnetic stirrer (6.5 pH), then 0.5 mg of triptorelin peptide was added. Finally, 0.15 mg of EDC (carbodiimide hydrochloride) and 0.09 mg of NHS (*N*-hydroxysulfosuccinimide) were added. The resulting mixture was stirred at room temperature for 2 hr. Finally, the resulting compounds were dialyzed for 24 hr in a refrigerator.

2.2. Characterization of NPs. A transmission electron microscope (Philips (CM120)) was used to determine the size and morphology of the Bi_2S_3@BSA NPs. X-ray diffraction is a fundamental and important characterization technique that is used to analysis of all materials. To confirm the Microstructure of NPs (GNR EXPLORER) with Cu-Kα radiation ($k = 1.542$ A) with the Bragg angle ranging from 10° to 80°, X-ray diffraction was used.

The zeta potential of NPs was measured using a nano/zeta sizer (HORIBA SZ100) with 25 scans in each spectrum, and the size of NPs was assessed by dynamic light scattering (HORIBA SZ100) in an aqueous solution. In addition, to measure nanoparticle stability in the cellular environment, Bi_2S_3@BSA–triptorelin NPs were suspended in the RPMI 1640 + 10% FBS and incubated for 24 hr at 37°C. Then the behavior of the Bi_2S_3@BSA–triptorelin NPs was measured by dynamic light scattering. Fourier transform infrared (FT-IR) spectroscopy was performed to determine the chemical structure of samples (Thermo Nicolet (AVATAR 370 FT-IR (USA))).

2.3. Cell Culture. Human breast adenocarcinoma (MCF-7) cell lines, obtained from the Pasteur Institute of Iran, were used in the in vitro study. MCF-7 cell lines were cultured in RPMI 1640 (Roswell Park Memorial Institute) supplemented with 10% fetal bovine serum (FBS) (Gibco, USA) and 1% penicillin-streptomycin (Gibco, USA). Subculturing of the MCF-7 cell lines was performed by detaching the adherent cells using 0.025% trypsin-EDTA (Gibco, USA). In order to wash the flask and remove the debris and floated dead cells, plates, and flasks were washed with phosphate-buffered saline (PBS) (Gibco, USA). Cells were incubated at 37°C with humidified 5% CO_2. In this study, before performing all the experiments, cells were carefully observed under a microscope. Also, all experiments were performed in the cell logarithmic growth stage.

2.4. Cytotoxicity Tests. Cytotoxicity test was performed by MTT (2,5-diphenyl-2H-tetrazolium bromide) assay as follows: an optimal number of MCF-7 cells were seeded in two 96-well plates (density of 104 per well [29]) and incubated in a RPMI 1640 supplemented with 10% FBS and 1% penicillin-streptomycin at 37°C and 5% CO_2 atmosphere 24 hr before treatment to allow attachment. The next step was to remove the culture medium and wash the plates with PBS. Then, the cells were incubated with 200 μl culture medium (5% FBS) per well containing Bi_2S_3@BSA, Bi_2S_3@BSA–triptorelin NPs at a series of concentrations (0 (control) 5, 10, 15, 25, 50, 75, 100, 150, and 200 μg/ml) for 24 hr. After that, the cells were washed twice with PBS, then were incubated with 90 μl of the fresh culture medium and 10 μl (5 mg/ml) of MTT (3-[4,5-dimethylthiazol-2-yl]-2,5-diphenyltetrazolium bromide) for 4 hr. Finally, MTT formazan crystals were dissolved in the medium by adding 200 μl dimethyl sulfoxide (DMSO). After that, the plate was placed on the orbital shaker for 20 min. The optical density (OD) was measured at 570 nm using a multiwall spectrophotometer (ELISA reader (Stat Fax 3200, Awareness Technology, USA)). The viability (%) of cells in different groups was calculated according to the following formula:

$$\text{Viability} = (\text{mean OD570 nm of the treated group/mean OD570 nm of the control group}) \times 100\%.$$

2.5. Irradiation. The cells were irradiated with megavoltage X-ray (6 MV) using Elekta Compact linear accelerator (Emam Reza Hospital, Mashhad, Iran) at a dose rate of 3 Gy/min with a field size of $20 \times 20\ \text{cm}^2$. In this study, we used five plexiglass (water equivalent) sheets with 1.5 cm thickness placed under the bottom of the plate to sufficiently production of backscatter.

2.6. Colony Formation Assay. The radiosensitivity caused by the presence of nanoparticles was assessed in MCF-7 cells by colony formation assay test. The colony-forming assay is the gold standard for measuring radiosensitivity. An appropriate number of MCF-7 cells (400, 1,000, 1,200, 1,400 for irradiation doses of 0, 2, 4, and 6 Gy, respectively) were seeded in 6-well plates and incubated in RPMI 1640 medium containing 10% FBS and 1% penicillin-streptomycin at 37°C in 5% CO_2 atmosphere 24 hr before treatment to allow attachment. Plates were divided into three groups: in the first group (without nanoparticles) medium was replaced with 3 ml of fresh medium. Second, the culture medium was replaced with fresh media containing Bi_2S_3@BSA at a concentration of 75 μg/ml. In the third group, the culture medium was replaced with the fresh media at a concentration of 75 μg/ml of Bi_2S_3@BSA-triptorelin, then incubated for 24 hr. Next, the medium inside each well of all plates was removed. The cells were washed twice with PBS, and 3 cc fresh culture medium (10% FBS) was added into each well. Then, the cells were exposed to radiation doses of 0, 2, 4, 6 Gy irradiated with 6 MV photon beams (Elekta Compact linear accelerator). Immediately after irradiation, the cells were incubated (10% FBS and 1% penicillin−streptomycin at 37°C in 5% CO_2) for ten days to allow colony formation. During this time, the medium was added to the plates as needed.

The colonies were fixed with methanol and acetic acid (3 : 1). Performed Giemsa staining after 24 hr. The colonies exceeding 50 cells were counted. The survival fraction (SF) was calculated using the following formula:

$$\text{SF} = \frac{\text{Number of colonies counted}}{\text{Number of cells cultured} \times \text{PE}/100}, \quad (1)$$

where

$$\text{PE (plate efficiency)} = \frac{\text{Number of colonies counted}}{\text{Number of cells cultured without any treatment}} \times 100. \quad (2)$$

The data fitted to the linear-quadratic model with the equation of SF = exp $(-\alpha D - \beta D2)$ and the survival curve were estimated using GraphPad Prism2018 software. In addition, α and β parameters of the survival curve were calculated with GraphPad Prism2018 software.

2.7. Apoptosis by Annexin-V FITC Assay. The two major mechanisms of cell death are apoptosis and necrosis. To determine the rate of apoptosis and quantify the number of apoptotic cells, flow cytometry (annexin V) was used. MCF-7 cells were cultured in 6-well plates at a density of 5,00,000 cells per well. Then were incubated (24 hr) in an RPMI 1640 medium containing 10% FBS and 1% penicillin–streptomycin at 37°C in a 5% CO_2 atmosphere. Briefly, the cells were treated with free nanoparticles, Bi_2S_3@BSA (75 μg/ml), and Bi_2S_3@BSA–triptorelin (75 μg/ml) for 24 hr. The culture medium of all wells of plates was removed. The cells were washed twice with PBS, and 3 cc fresh culture medium (10% FBS) was added to each well. Then, the cells were exposed to radiation doses of 0, 2, 4, 6 Gy with 6 MV photon beams (Elekta Compact linear accelerator). After 24 hr, the cells were trypsinized and washed twice in PBS. After that, the harvested cells were collected by centrifugation at 1,500 rpm for 3 min, then resuspended in 0.5 ml binding buffer. The cell suspension was incubated with 7 μl annexin V-FITC for 15 min and 5 μl PI for 5 min at room temperature in the dark. Finally, the samples (stained cells) were analyzed immediately with flow cytometry (BD Accuri C6). Quantification of results was performed using Flowjo 7.6 software. Viable cells were identified with negative cells of annexin V-FITC and PI; early apoptotic cells were identified with annexin V-FITC positive cells; late apoptotic cells were identified with positive annexin V-FITC and PI cells; finally, to determine necrotic cells, positive PI and negative annexin cells were considered.

2.8. Statistical Analysis. GraphPad Prism2018 software was used to perform statistical analysis. Differences in percentage cell viability between groups were analyzed by one-way ANOVA and Tukey's multiple comparison tests ($P < 0.05$). All graphs were plotted by using GraphPad Prism2018 software.

3. Result

3.1. Characteristics. Figure 2(a) shows the transmission electron microscopy (TEM) image of Bi_2S_3@BSA NPs. The morphology of Bi_2S_3@BSA NPs was spherical. The average size was 8.649 ± 1.69 nm. Figure 2(b)–2(g) shows the size distribution and zeta potential of Bi_2S_3@BSA and Bi_2S_3@BSA–triptorelin NPs. The average sizes of Bi_2S_3@BSA and Bi_2S_3@BSA–triptorelin NPs were about 16 ± 2 nm and 17.1 ± 2 nm, with a zeta potential of -77.8 ± 3.80 mV and -84.7 ± 2.18 mV. The poly index of Bi_2S_3@BSA was 0.623 ± 0.033. The average size of Bi_2S_3 NPs was 14.2 nm with a zeta potential of -69.8 ± 2.90 mV. Moreover, the results showed that the hydrodynamic size of Bi_2S_3@BSA–triptorelin NPs after 24 hr incubation was 17.3 ± 1.1 nm, which showed good stability in the cellular environment. All diffraction peaks of Bi_2S_3@BSA NPs almost demonstrated the Bi_2S_3 structure (JCPDS No. 43-1471) [30]. According to the XRD (X-ray powder diffraction) pattern, all the peaks were well indexed to the orthorhombic Bi_2S_3 crystal (Figure 3(a)) because Bi_2S_3 NPs coated with BSA, Bi_2S_3@BSA NPs are not exactly in agreement with the standard card (peak in the areas of 20°–30° is related to the BSA) [31]. To confirm the conjugation of triptorelin on the surface of Bi_2S_3@BSA NPs, FT-IR spectroscopy was done. Figure 3(b) shows the FT-IR spectrum of functionalized Bi_2S_3@BSA and Bi_2S_3@BSA–triptorelin NPs. The formation of peaks 1,651 and 1,576 cm^{-1} is related to primary and secondary amide and amine bonds. It shows the presence of BSA on the nanoparticle surface. The removal of the thiol peak at 2,360 cm^{-1} is due to the presence of a complex between bismuth and thiol, which leads to the formation of a bismuth–sulfur bond; finally, a sulfide bond is obtained. Peak 670 cm^{-1} could also be related to bismuth sulfide bonding. The peptide binds to the nanoparticle surface via an amide bond. Due to the presence of BSA on the nanoparticle surface, amide bonds appeared together in 1,663 cm^{-1} because of the new amid bonds that were in accordance with redshift. Peak 1,651 cm^{-1}, which corresponds to the BSA amide peak, disappeared and changed to peak 1,633 cm^{-1} due to the amide bond between triptorelin and BSA. The presence of peak 702 cm^{-1} indicates the bonding of aromatic hydrocarbon, which is related to the aromatic ring of the triptorelin peptide compound.

3.2. In Vitro Cytotoxicity Assay. The cytotoxicity of NPs was measured by the MCF-7 cell line. The MCF-7 cell line was treated with Bi_2S_3@BSA NPs, Bi_2S_3@BSA–triptorelin NPs at different concentrations (0, 5, 10, 15, 25, 50, 100, 150, and 200 μg/ml) for 24 hr. Figure 4 shows the percentage cell viability of the MCF-7 cell lines incubated with NPs at different concentrations.

The results of the MTT test presented the viability of cells incubated with Bi_2S_3@BSA and Bi_2S_3@BSA–triptorelin at different concentrations. There were no significant differences (not toxic) between the control and test groups ($P < 0.05$) up to 150 and 75 μg/ml, respectively. Since the purpose of this study was to use Bi_2S_3@BSA as a radiosensitizer with low toxicity, concentrations of 75 μg/ml were used for colony and apoptosis assay.

3.3. In Vitro Radiosensivity Assay. In order to investigate the effect of nanoparticles as a radiosensitizer, colony formation

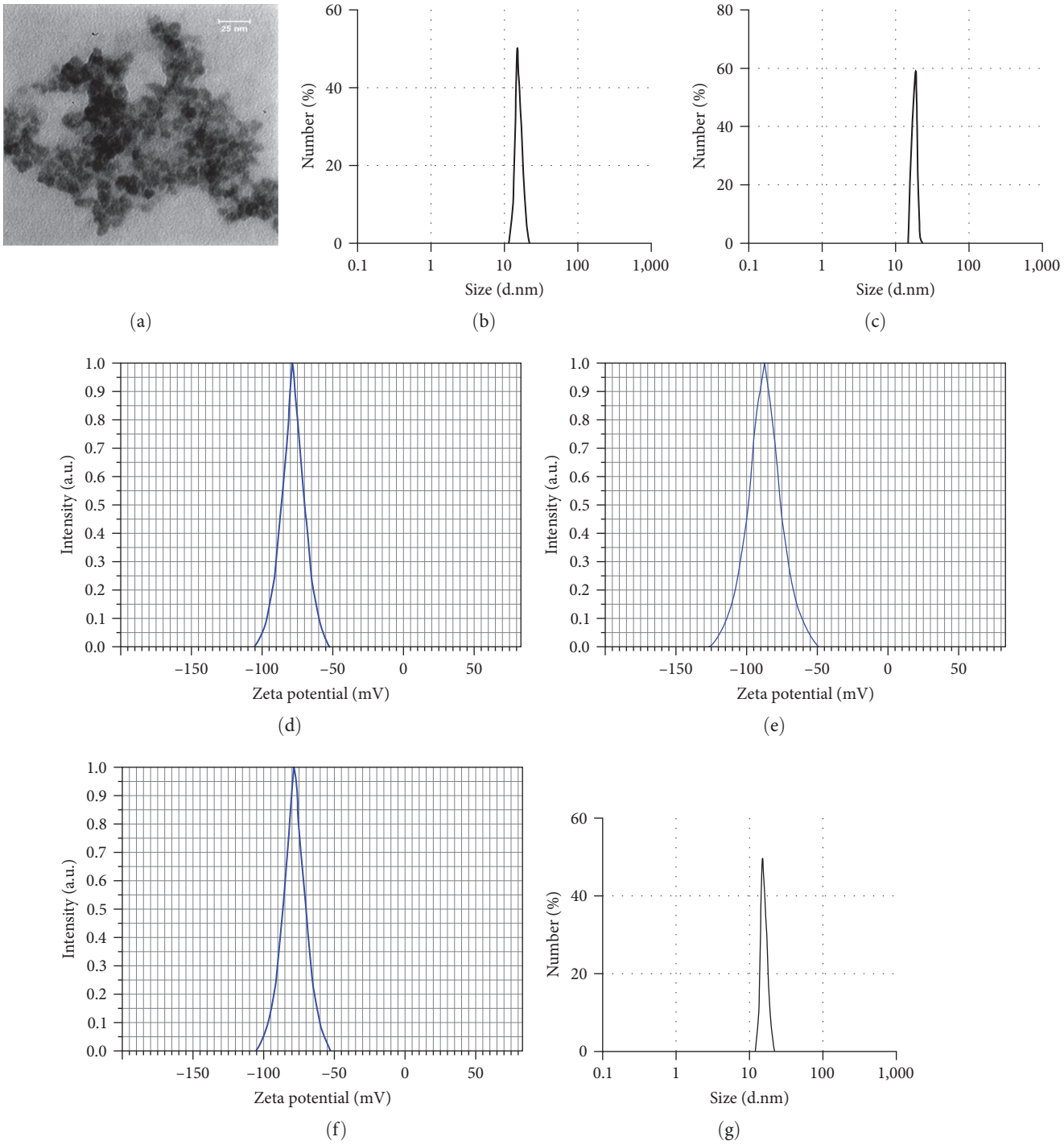

FIGURE 2: (a) TEM image of Bi_2S_3@BSA NPs, (b) and (c) size distribution and (d) and (e) zeta potential of Bi_2S_3@BSA NPs and Bi_2S_3@BSA–triptorelin NPs, (f) and (g) shows zeta potential and size distribution of Bi_2S_3 NPs.

assay as the "Gold Standard" of radiosensitivity was performed, and the survival curve was plotted (Figure 5 (vertical axis at logarithmic scale)). The results showed that a nontoxic concentration of nanoparticles (75 μg/ml) at RT reduced the viability of MCF7 cells. The viability of cells treated with Bi_2S_3@BSA–triptorelin, Bi_2S_3@BSA, and cells that were not treated with nanoparticles at all doses was significantly decreased ($P<0.05$). SFs for groups of cells not treated with nanoparticles and were just exposed to radiation doses 2, 4, and 6 Gy, also radiation as well as triptorelin (irradiated with 6 MV photon beams), were 79.49%, 54.21%, 22.24%, and 79.1%, 54.6%, 21.9%, respectively. There was no difference between the groups of cells treated with radiation alone and radiation plus triptorelin ($P<0.05$). In the presence of Bi_2S_3@BSA (75 μg/ml), they were 53%, 31%, and 12%, respectively, and decreased to 35%, 12.5%, and 2% in the

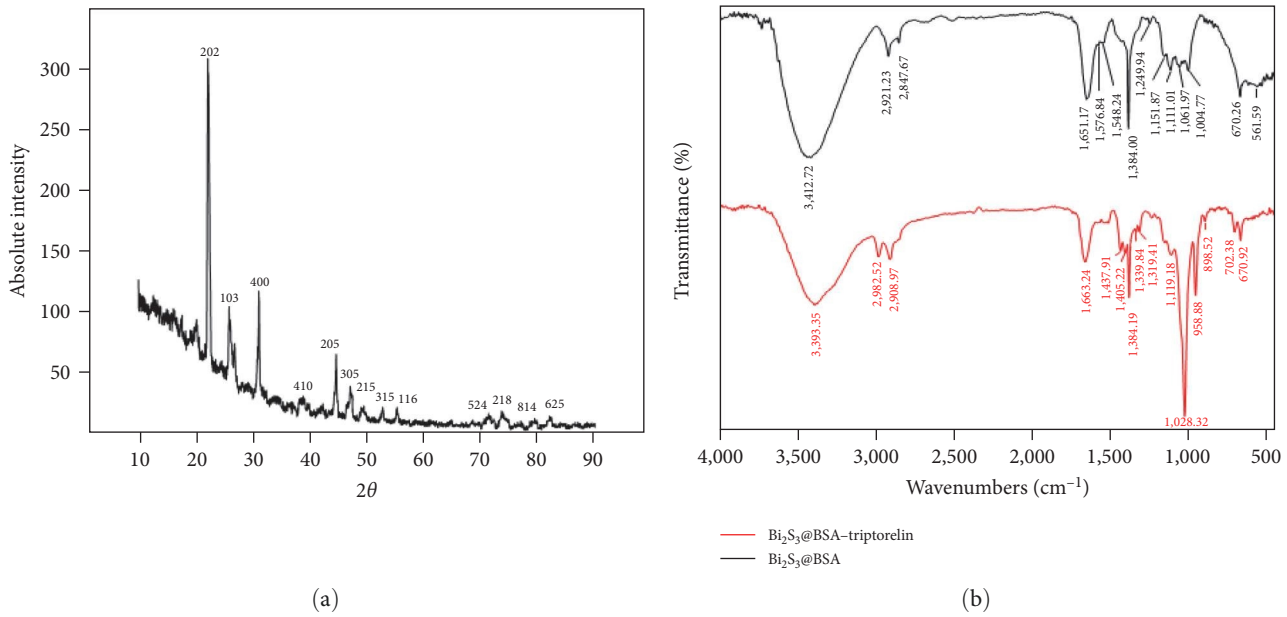

FIGURE 3: (a) X-ray diffraction pattern of Bi_2S_3@BSA, (b) Fourier transform infrared spectra of Bi_2S_3@BSA NPs, Bi_2S_3@BSA–triptorelin.

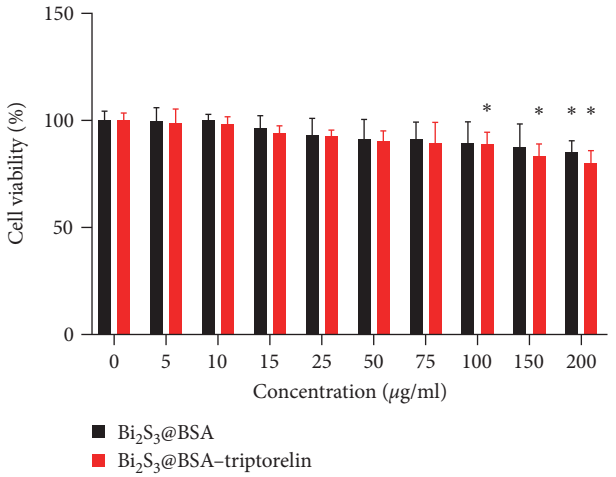

FIGURE 4: Percentage cell viability of the MCF-7 cells incubated with different concentrations of Bi_2S_3@BSA NPs and Bi_2S_3@BSA–triptorelin NPs. Error bars indicate the standard error of the mean (SEM) for $n = 3$ independent experiments. *Indicates significant difference with $P < 0.05$.

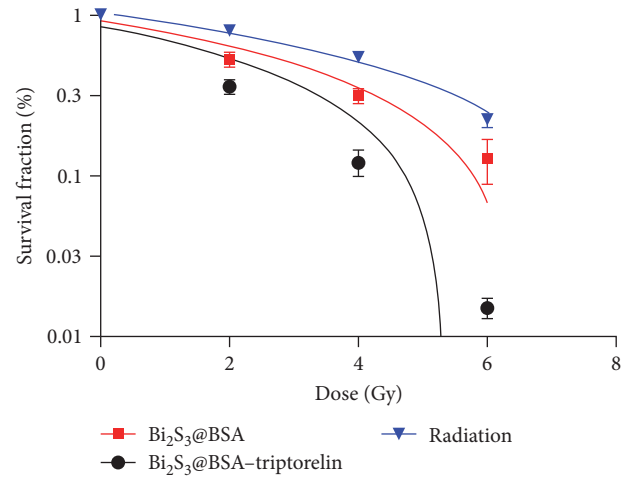

FIGURE 5: Survival curves of MCF-7 cells with 75 μg/ml concentrations of Bi_2S_3@BSA NPs and Bi_2S_3@BSA–triptorelin NPs irradiated with 6 MV. Error bars indicate the standard error of the mean (SEM) for $n = 3$ independent experiments.

presence of Bi_2S_3@BSA–triptorelin. Table 1 shows α and β parameters of the survival curve for different groups.

3.4. Effects of NPs on MCF-7 Cell Apoptosis. In the current study, to investigate the mechanism of nanoparticle radiosensitivity, annexin V-FITC/PI staining was used. The result indicated that when cells were treated with Bi_2S_3@BSA–triptorelin (75 μg/ml) of nanoparticles in combination with radiation, apoptotic percentage induced in the MCF-7 cells was significantly higher compared to cells treated with Bi_2S_3@BSA and radiation ($P < 0.05$). In addition, MCF-7 cells treated with Bi_2S_3@BSA and exposed to 6 MV irradiation induced a significant increase in apoptosis compared to MCF-7 cells irradiated alone. There was no difference between the groups of cells treated with radiation alone and radiation plus triptorelin ($P < 0.05$). Figures 6 and 7 show the result of flow cytometry. Percentages of necrotic cells were not significantly different among the cells treated with targeted and nontargeted nanoparticles in combination with RT or those treated with radiation alone.

4. Discussion

It is usually suggested that one crucial factor that affects cytotoxicity is nanoparticle size. Smaller nanoparticles have a larger surface-area-to-volume ratio and could decrease cell

Table 1: Values of α, β ($\pm$SD) of MCF-7 cells in different groups.

Groups	α (Gy^{-1})	β (Gy^{-2})
Radiation	0.08626 ± 0.01019	0.007169 ± 0.001628
Radiation + Bi_2S_3@BSA	0.2226 ± 0.02893	0.01284 ± 0.004621
Radiation + Bi_2S_3@BSA–triptorelin	0.3623 ± 0.01442	0.03375 ± 0.002304

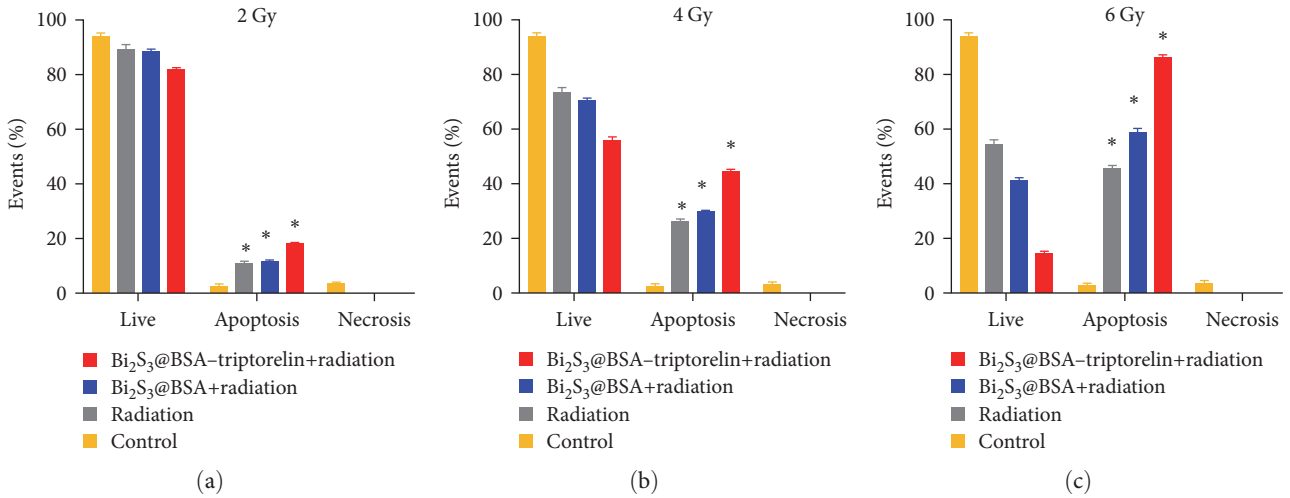

Figure 6: Percentage (%) of living, apoptotic, and necrotic in MCF-7 cells treated or not treated with Bi_2S_3@BSA NPs and Bi_2S_3@BSA–triptorelin induced after (a) 2 Gy, (b) 4 Gy, and (c) 6 Gy radiation doses and control (no any treatment. Error bars indicate the standard error of the mean (SEM) for $n = 3$ independent experiments. *indicates significant difference with $P < 0.05$.

viability. Many studies also show that the cytotoxicity of several types of nanoparticles was size-dependent [32]. A study by Algethami et al. [33] investigated the toxicity of Bi_2S_3 (PVP coated) nanoparticles with a diameter of 3–5 nm on PC3 cell lines for 48hr. Even at concentrations of 0.5 mM, the nanoparticles are not toxic. Our results show that in MCF-7 cells treated with different concentrations of Bi_2S_3@BSA, no significant toxicity was observed, even up to 150 μg/ml concentration. This difference could be due to the surface coating of the nanoparticles and the type of cell line used for the experiment. In the study of Azizi et al. [34], the cytotoxicity of Bi_2S_3@BSA nanoparticles with a hydrodynamic size of 107.6 ± 6.81 nm on 4T1 cell lines was evaluated, and the viability of the 4T1 cells treated with Bi_2S_3@BSA (200 μg/ml) nanoparticles was significantly reduced, which almost follow the results of our study. In addition, there are no appropriate studies to compare the biocompatibility of nanoparticles in this study, as the toxicity of Bi-based compounds varies with cell lines and concentrations. Also, other studies have shown that BSA improves the biocompatibility of Bi_2S_3 nanoparticles [35–37].

The radiosensitivity effect of nanoparticles in combination with high energy is suggested in nanoparticle-treated cells [38, 39]. Recently, bismuth-based nanomaterials have demonstrated their ability to increase radiation dose, their application in multimodal imaging, their ability to act as computed tomography (CT) contrast agents, and their biocompatibility [40]. The results of this study demonstrate that Bi_2S_3@BSA increases the radiosensitivity of MCF-7 cells at all doses using low linear energy transfer. Our results are consistent with Ma et al.'s [41] study, which treated PC3 cells with Bi_2S_3-embedded mesoporous silica nanoparticles and investigated the radiosensitizing effects of these nanoparticles in radionuclide combination therapy (P-32). They suggested that the inhibition rate of the cell group treated with P-32 treatment was only 16.1% (24 hr), whereas the inhibition rate after treatment with nanoparticles (50 μg/ml) and RT was 57% (24 hr), which was significantly enhanced. These results are supported by Huang et al. [42]. They reported less than 20% cell inhibition (after 48 hr) in the PC3 cell line (P-32) treated with radiation. While Bi_2S_3-PLGA capsules (200 μg/ml) and irradiation (P-32) resulted in greater than 30% cell inhibition. Finally, declared that cell inhibition is a concentration-dependent cell inhibition in the PC3 cell lines. Apart from that, Azizi et al. [34] observed that Bi_2S_3@BSA nanoparticles as radiosensitizers increased the sensitivity of cancer cells to radiation. Given the radiosensitivity effects of Bi_2S_3 nanoparticles at megavoltage energies, there is a report published by Abhari et al. [43]. They reported that increasing concentrations of Bi_2S_3-BSA enhanced the inhibition of cell proliferation (4T1). Other studies on the use of Bi_2S_3 nanoparticles in RT have been limited to kilovoltage energies. This study may provide researchers with useful data in the field of radiosensitivity of bismuth-based nanoparticles at megavoltage energies.

This in vitro study demonstrated that nontoxic concentrations of bovine serum albumin-coated Bi_2S_3 nanoparticles significantly ($P < 0.05$) induced radiosensitivity in the MCF-7 cell line when exposed to MV X-rays at all doses. These

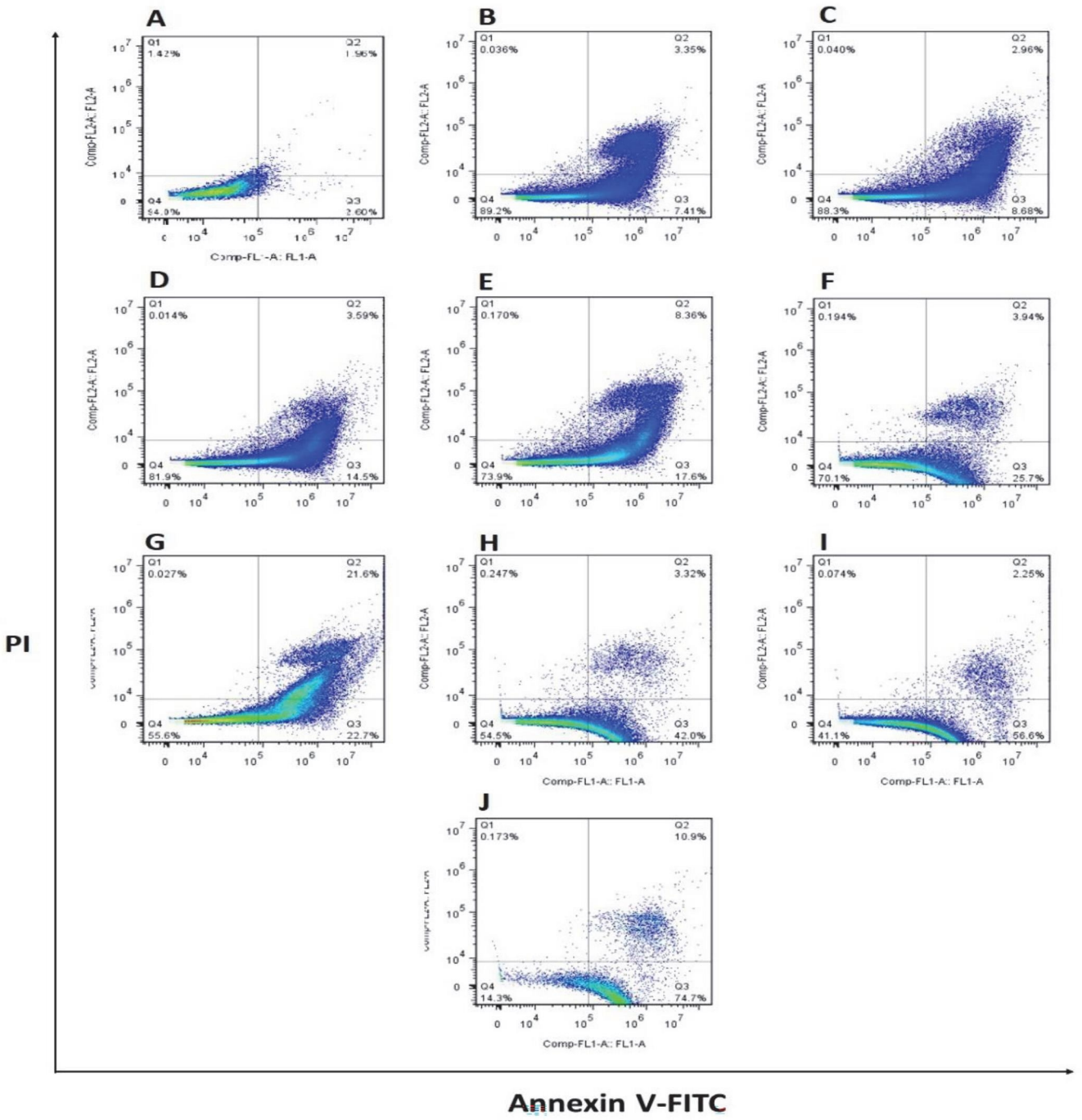

Figure 7: Flow cytometry analysis of apoptosis in MCF-7 cells stained with annexin V-FITC and PI: (a) control (no treatment), (b) X-ray alone (2 Gy), (c) X-ray (2 Gy) + Bi_2S_3@BSA, (d) X-ray (2 Gy) + Bi_2S_3@BSA–triptorelin, (e) X-ray alone (4 Gy), (f) X-ray (4 Gy) + Bi_2S_3@BSA, (g) X-ray (4 Gy) + Bi_2S_3@BSA–triptorelin, (h) X-ray alone (6 Gy), (i) X-ray (6 Gy) + Bi_2S_3@BSA, (j) X-ray (6 Gy) + Bi_2S_3@BSA–triptorelin.

results are fully consistent with the study by Abhari et al. [43]. The study conducted by Ai et al. [44] suggested that Bi_2S_3 NPs are internalized into cells via endocytosis. This enhancement in radiosensitivity can be attributed to the fact that the internalized NPs in target cells in interaction with ionization radiation may produce high numbers of free radicals through photoelectric and Compton interactions. These additional free radicals would increase the probability of DNA damage and subsequent cell death, thus enhancing the radiosensitivity [33]. The surviving fractions of MCF-7 cells were determined to assess the radiosensitization effect of nanoparticles. Colony formation assay results showed significantly lower viability of MCF-7 cells treated with Bi_2S_3@BSA-triptorelin nanoparticles + X-rays at all doses compared to Bi_2S_3@BSA nanoparticles + X-rays ($P < 0.05$). Also, the decrease in viability of targeted and nontargeted

nanoparticles was dependent on the X-ray exposure dose. Maybe the triptorelin conjugated with Bi_2S_3@BSA could enhance the internalization of Bi_2S_3@BSA nanoparticles through the GnRH receptors in MCF-7 cells. A parallel study by Mohammadi et al. [45] was performed on bismuth sulfide nanoparticles coated with BSA and targeted with a triptorelin peptide (nanoparticles similar to this study). CT imaging was used to identify differences in MCF-7 cellular uptake between targeted and nontargeted nanoparticles at 75 μg/ml concentration at 90 kVp; the X-ray attenuation intensity of cells in the presence of targeted nanoparticles is 1.4 times greater than cells in the presence of nontargeted nanoparticles, which indicates an increase in the uptake of targeted nanoparticles by MCF-7 cells.

Zoghi et al. [46] showed that the biodistribution of a tracer targeted by triptorelin showed significant uptake in tumors expressing GnRH receptors. The results of our study in this section are consistent with those obtained by Yu et al. [47]. Their results showed Bi-NPs exhibited higher tumor accumulation after binding with the tumor-homing peptide LyP-1. BiLyP-1 NPs exhibited a significant radiosensitizing effect in interaction with ionizing radiation (because of more internalization into cells). Also, our results are in agreement with the Obayemi et al. [48] report, which demonstrated that LHRH-conjugated nanoparticles specifically bind to receptors overexpressed on the surface of most breast cancer cell types.

After treatment, the flow cytometry analyses on MCF-7 cells were performed to investigate the possible mechanism of radiosensitivity. Our results (Figures 6 and 7) showed that the amount of apoptosis was significantly higher than that of necrosis in all groups. This observation may introduce apoptosis as the major mechanism that determines radiosensitivity. Our results were consistent with those obtained by Ma et al. [41]. They introduced apoptosis as mainly contributing to the antiproliferative effects of Bi_2S_3-embedded mesoporous silica nanoparticles in combination with P-32 radiation. Li et al. [49] suggested that in 4T1 cells treated with Fe@Bi_2S_3 + radiation, apoptosis more than necrosis induces cell death, which is consistent with our results. In our study, targeted nanoparticles compared to nontargeted induced significantly more apoptosis nanoparticles ($P<0.05$), which confirmed the colony formation assay results. In this study, we observed an increase in radiosensitization by targeted nanoparticles. It can be inferred that apoptosis was related to the radiosensitivity and cell death induced by nanoparticles plus radiation. More studies are needed to specify the role of nanoparticles in biological pathways affecting apoptosis and other biological interactions.

5. Conclusion

For the first time, novel targets based on Bi_2S_3@BSA and triptorelin were developed using an inexpensive functionalization process with a spherical shape, small size, and appropriate zeta potential to improve quality and reduce breast cancer radiotherapy side effects. In this study, we have successfully improved the stability of Bi_2S_3 nanoparticles by using BSA because of its chemical stability and nontoxicity. Bi_2S_3@BSA conjugated with triptorelin can target the GnRH receptors expressed on breast cancer cells membrane. The toxic effect of Bi_2S_3@BSA nanoparticles conjugated with triptorelin on the MCF-7 cell lines under megavoltage X-ray radiation demonstrated that Bi_2S_3@BSA–triptorelin nanoparticles, as a targeted radiosensitizer, increased the radiosensitivity of breast cancer cells. These properties of nanoparticles have raised the possibility of using them as a promising candidate for in vitro and in vivo (in future studies) therapeutic experiments aimed at developing and achieving cancer medication for cancer therapy.

Data Availability

The data presented in this study are available on request from the corresponding authors.

Conflicts of Interest

The authors declare that they have no conflicts of interest.

Funding

This article is based on the results exploited from an M.Sc. thesis (Code: 971956) that is supported by the Medical Physics Department of Mashhad University of Medical Sciences.

Acknowledgments

The authors would like to thank all members of the Medical Physics Department of Mashhad University of Medical Sciences.

References

[1] R. Bazak, M. Houri, S. El Achy, W. Hussein, and T. Refaat, "Passive targeting of nanoparticles to cancer: a comprehensive review of the literature," *Molecular and Clinical Oncology*, vol. 2, no. 6, pp. 904–908, 2014.

[2] M. M. Fathy, F. S. Mohamed, N. S. Elbialy, and W. M. Elshemey, "Multifunctional chitosan-capped gold nanoparticles for enhanced cancer chemo-radiotherapy: an invitro study," *Physica Medica*, vol. 48, pp. 76–83, 2018.

[3] A. Rajaee, S. Wang, L. Zhao et al., "Multifunction bismuth gadolinium oxide nanoparticles as radiosensitizer in radiation therapy and imaging," *Physics in Medicine & Biology*, vol. 64, Article ID 195007, 2019.

[4] L. Cui, S. Her, G. R. Borst, R. G. Bristow, D. A. Jaffray, and C. Allen, "Radiosensitization by gold nanoparticles: will they ever make it to the clinic?" *Radiotherapy and Oncology*, vol. 124, no. 3, pp. 344–356, 2017.

[5] Z. Rezaee, A. Yadollahpour, V. Bayati, and F. N. Dehbashi, "Gold nanoparticles and electroporation impose both separate and synergistic radiosensitizing effects in HT-29 tumor cells: an in vitro study," *International Journal of Nanomedicine*, vol. 12, pp. 1431–1439, 2017.

[6] J. Deng, S. Xu, W. Hu, X. Xun, L. Zheng, and M. Su, "Tumor targeted, stealthy and degradable bismuth nanoparticles for enhanced X-ray radiation therapy of breast cancer," *Biomaterials*, vol. 154, pp. 24–33, 2018.

[7] J. F. Hainfeld, F. Avraham Dilmanian, D. N. Slatkin, and H. M. Smilowitz, "Radiotherapy enhancement with gold nanoparticles," *Journal of Pharmacy and Pharmacology*, vol. 60, no. 8, pp. 977–985, 2008.

[8] G. Gordon Steel and M. J. Peckham, "Exploitable mechanisms in combined radiotherapy-chemotherapy: the concept of additivity," *International Journal of Radiation Oncology Biology Physics*, vol. 5, no. 1, pp. 85–91, 1979.

[9] T. Cardilin, J. Almquist, M. Jirstrand, A. Zimmermann, S. El Bawab, and J. Gabrielsson, "Model-based evaluation of radiation and radiosensitizing agents in oncology," *CPT: Pharmacometrics & Systems Pharmacology*, vol. 7, no. 1, pp. 51–58, 2018.

[10] M.-T. Bahreyni-Toossi, E. Dolat, H. Khanbabaei, N. Zafari, and H. Azimian, "microRNAs: potential glioblastoma radiosensitizer by targeting radiation-related molecular pathways," *Mutation Research/Fundamental and Molecular Mechanisms of Mutagenesis*, vol. 816-818, Article ID 111679, 2019.

[11] P. Wardman, "Chemical radiosensitizers for use in radiotherapy," *Clinical Oncology*, vol. 19, no. 6, pp. 397–417, 2007.

[12] A.-L. Papa, S. Basu, P. Sengupta, D. Banerjee, S. Sengupta, and R. Harfouche, "Mechanistic studies of gemcitabine-loaded nanoplatforms in resistant pancreatic cancer cells," *BMC Cancer*, vol. 12, Article ID 419, 2012.

[13] J. Xie, L. Gong, S. Zhu, Y. Yong, Z. Gu, and Y. Zhao, "Emerging strategies of nanomaterial-mediated tumor radiosensitization," *Advanced Materials*, vol. 31, no. 3, Article ID 1802244, 2019.

[14] C. Stewart, K. Konstantinov, S. McKinnon et al., "First proof of bismuth oxide nanoparticles as efficient radiosensitisers on highly radioresistant cancer cells," *Physica Medica*, vol. 32, no. 11, pp. 1444–1452, 2016.

[15] R. Zhou, X. Liu, Y. Wu et al., "Suppressing the radiation-induced corrosion of bismuth nanoparticles for enhanced synergistic cancer radiophototherapy," *ACS Nano*, vol. 14, no. 10, pp. 13016–13029, 2020.

[16] L. Jiao, Q. Li, J. Deng, N. Okosi, J. Xia, and M. Su, "Nanocellulose templated growth of ultra-small bismuth nanoparticles for enhanced radiation therapy," *Nanoscale*, vol. 10, no. 14, pp. 6751–6757, 2018.

[17] A. L. Brown and A. M. Goforth, "pH-dependent synthesis and stability of aqueous, elemental bismuth glyconanoparticle colloids: potentially biocompatible X-ray contrast agents," *Chemistry of Materials*, vol. 24, no. 9, pp. 1599–1605, 2012.

[18] M. Hossain and M. Su, "Nanoparticle location and material-dependent dose enhancement in X-ray radiation therapy," *The Journal of Physical Chemistry C*, vol. 116, no. 43, pp. 23047–23052, 2012.

[19] X.-D. Zhang, Z. Luo, J. Chen et al., "Ultrasmall $Au_{10-12}(SG)_{10-12}$ nanomolecules for high tumor specificity and cancer radiotherapy," *Advanced Materials*, vol. 26, no. 26, pp. 4565–4568, 2014.

[20] A. V. Schally and A. Nagy, "Chemotherapy targeted to cancers through tumoral hormone receptors," *Trends in Endocrinology & Metabolism*, vol. 15, no. 7, pp. 300–310, 2004.

[21] Ž. Krpetić, S. Anguissola, D. Garry, P. M. Kelly, and K. A. Dawson, "Nanomaterials: impact on cells and cell organelles," in *Nanomaterial*, D. Capco and Y. Chen, Eds., vol. 811 of *Advances in Experimental Medicine and Biology*, pp. 135–156, Springer, Dordrecht, 2014.

[22] E. Mahon, A. Salvati, F. B. Bombelli, I. Lynch, and K. A. Dawson, "Designing the nanoparticle–biomolecule interface for "targeting and therapeutic delivery"," *Journal of Controlled Release*, vol. 161, no. 2, pp. 164–174, 2012.

[23] R. C. Ladner, A. K. Sato, J. Gorzelany, and M. de Souza, "Phage display-derived peptides as therapeutic alternatives to antibodies," *Drug Discovery Today*, vol. 9, no. 12, pp. 525–529, 2004.

[24] S. M. P. Vadevoo, S. Gurung, F. Khan et al., "Peptide-based targeted therapeutics and apoptosis imaging probes for cancer therapy," *Archives of Pharmacal Research*, vol. 42, pp. 150–158, 2019.

[25] N. Zhao, Z. Yang, B. Li et al., "RGD-conjugated mesoporous silica-encapsulated gold nanorods enhance the sensitization of triple-negative breast cancer to megavoltage radiation therapy," *International Journal of Nanomedicine*, vol. 11, pp. 5595–5610, 2016.

[26] X. Deng, Q. Qiu, K. Ma, W. Huang, and H. Qian, "Synthesis and in vitro anti-cancer evaluation of luteinizing hormone-releasing hormone-conjugated peptide," *Amino Acids*, vol. 47, pp. 2359–2366, 2015.

[27] A. R. Günthert, C. Gründker, A. Olota, J. Läsche, N. Eicke, and G. Emons, "Analogs of GnRH-I and GnRH-II inhibit epidermal growth factor-induced signal transduction and resensitize resistant human breast cancer cells to 4OH-tamoxifen," *European Journal of Endocrinology*, vol. 153, no. 4, pp. 613–625, 2005.

[28] M. Fekete, J. L. Wittliff, and A. V. Schally, "Characteristics and distribution of receptors for [d-trp^6]-luteinizing hormone-releasing hormone, somatostatin, epidermal growth factor, and sex steroids in 500 biopsy samples of human breast cancer," *Journal of Clinical Laboratory Analysis*, vol. 3, no. 3, pp. 137–147, 1989.

[29] R. Wahab, M. A. Siddiqui, Q. Saquib et al., "ZnO nanoparticles induced oxidative stress and apoptosis in HepG2 and MCF-7 cancer cells and their antibacterial activity," *Colloids and Surfaces B: Biointerfaces*, vol. 117, pp. 267–276, 2014.

[30] Y. Wang, Y. Wu, Y. Liu et al., "BSA-mediated synthesis of bismuth sulfide nanotheranostic agents for tumor multimodal imaging and thermoradiotherapy," *Advanced Functional Materials*, vol. 26, no. 29, pp. 5335–5344, 2016.

[31] P. Yang, Q. Liu, J. Liu et al., "Bovine serum albumin-coated graphene oxide for effective adsorption of uranium (VI) from aqueous solutions," *Industrial & Engineering Chemistry Research*, vol. 56, no. 13, pp. 3588–3598, 2017.

[32] N. N. T. Sisin, S. Z. Abidin, M. A. Yunus, H. M. Zin, K. A. Razak, and W. N. Rahman, "Evaluation of bismuth oxide nanoparticles as radiosensitizer for megavoltage radiotherapy," *International Journal on Advanced Science, Engineering and Information Technology*, vol. 9, no. 4, pp. 1434–1443, 2019.

[33] M. Algethami, M. Geso, T. Piva et al., "Radiation dose enhancement using Bi_2S_3 nanoparticles in cultured mouse PC3 prostate and B16 melanoma cells," *NanoWorld Journal*, vol. 1, no. 2, 2015.

[34] S. Azizi, H. Nosrati, A. Sharafi, and H. Danafar, "Preparation of bismuth sulfide nanoparticles as targeted biocompatible nano-radiosensitizer and carrier of methotrexate," *Applied Organometallic Chemistry*, vol. 34, no. 1, Article ID e5251, 2020.

[35] M. H. Faghfoori, H. Nosrati, H. Rezaeejam et al., "Anticancer effect of X-Ray triggered methotrexate conjugated albumin coated bismuth sulfide nanoparticles on SW480 colon cancer cell line," *International Journal of Pharmaceutics*, vol. 582, Article ID 119320, 2020.

[36] H. Nosrati, F. Abhari, J. Charmi et al., "Facile green synthesis of bismuth sulfide radiosensitizer *via* biomineralization of albumin natural molecule for chemoradiation therapy aim,"

Artificial Cells, Nanomedicine, and Biotechnology, vol. 47, no. 1, pp. 3832–3838, 2019.

[37] H. Nosrati, E. Attari, F. Abhari et al., "Complete ablation of tumors using synchronous chemoradiation with bimetallic theranostic nanoparticles," *Bioactive Materials*, vol. 7, pp. 74–84, 2022.

[38] F. Geng, K. Song, J. Z. Xing et al., "Thio-glucose bound gold nanoparticles enhance radio-cytotoxic targeting of ovarian cancer," *Nanotechnology*, vol. 22, no. 28, Article ID 285101, 2011.

[39] C. Wang, X. Li, Y. Wang, Z. Liu, L. Fu, and L. Hu, "Enhancement of radiation effect and increase of apoptosis in lung cancer cells by thio-glucose-bound gold nanoparticles at megavoltage radiation energies," *Journal of Nanoparticle Research*, vol. 15, Article ID 1642, 2013.

[40] X. Cheng, Y. Yong, Y. Dai et al., "Enhanced radiotherapy using bismuth sulfide nanoagents combined with photothermal treatment," *Theranostics*, vol. 7, no. 17, pp. 4087–4098, 2017.

[41] M. Ma, Y. Huang, H. Chen et al., "Bi_2S_3-embedded mesoporous silica nanoparticles for efficient drug delivery and interstitial radiotherapy sensitization," *Biomaterials*, vol. 37, pp. 447–455, 2015.

[42] Y. Huang, M. Ma, S. Chen, J. Dai, F. Chen, and Z. Wang, "Construction of multifunctional organic–inorganic hybrid Bi_2S_3-PLGA capsules for highly efficient ultrasound-guided radiosensitization of brachytherapy," *RSC Advances*, vol. 4, no. 51, pp. 26861–26865, 2014.

[43] F. Abhari, J. Charmi, H. Rezaeejam et al., "Folic acid modified bismuth sulfide and gold heterodimers for enhancing radiosensitization of mice tumors to X-ray radiation," *ACS Sustainable Chemistry & Engineering*, vol. 8, no. 13, pp. 5260–5269, 2020.

[44] K. Ai, Y. Liu, J. Liu, Q. Yuan, Y. He, and L. Lu, "Large-scale synthesis of Bi_2S_3 nanodots as a contrast agent for in vivo X-ray computed tomography imaging," *Advanced Materials*, vol. 23, no. 42, pp. 4886–4891, 2011.

[45] M. Mohammadi, S. Khademi, Y. Choghazrdi, R. Irajirad, M. Keshtkar, and A. Montazerabadi, "Modified bismuth nanoparticles: a new targeted nanoprobe for computed tomography imaging of cancer," *Cell Journal (Yakhteh)*, vol. 24, no. 9, pp. 515–521, 2022.

[46] M. Zoghi, A. R. Jalilian, A. Niazi, F. Johari-Daha, B. Alirezapour, and S. Ramezanpour, "Development of a ^{68}Ga-peptide tracer for PET GnRH1-imaging," *Annals of Nuclear Medicine*, vol. 30, pp. 400–408, 2016.

[47] X. Yu, A. Li, C. Zhao, K. Yang, X. Chen, and W. Li, "Ultrasmall semimetal nanoparticles of bismuth for dual-modal computed tomography/photoacoustic imaging and synergistic thermoradiotherapy," *ACS Nano*, vol. 11, no. 4, pp. 3990–4001, 2017.

[48] J. D. Obayemi, S. Dozie-Nwachukwu, Y. Danyuo et al., "Biosynthesis and the conjugation of magnetite nanoparticles with luteinizing hormone releasing hormone (LHRH)," *Materials Science and Engineering: C*, vol. 46, pp. 482–496, 2015.

[49] E. Li, X. Cheng, Y. Deng et al., "Fabrication of PEGylated Fe@Bi_2S_3 nanocomposites for dual-mode imaging and synergistic thermoradiotherapy," *Biomaterials Science*, vol. 6, no. 7, pp. 1892–1898, 2018.

Hindawi
Journal of Nanomaterials
Volume 2023, Article ID 8812824, 10 pages
https://doi.org/10.1155/2023/8812824

Research Article

Hydroxyl Radical Generating Monovalent Copper Particles for Antimicrobial Application

Tze Hao Tan,[1] **Hao Zhang**,[1] **Bingqiao Xie**,[1] **Riti Mann**,[2] **Lingyi Peng**,[1] **Sung Lai Jimmy Yun**,[3] **Rose Amal**,[1] **Zi Gu**,[1] **and Cindy Gunawan**[2]

[1]*School of Chemical Engineering, UNSW Sydney, Sydney, NSW 2052, Australia*
[2]*Australian Institute for Microbiology and Infection, University of Technology Sydney, Ultimo, NSW 2007, Australia*
[3]*Qingdao International Academician Park Research Institute, Qingdao 266000, Shandong, China*

Correspondence should be addressed to Tze Hao Tan; tzehaotan@gmail.com, Zi Gu; zi.gu1@unsw.edu.au and Cindy Gunawan; cindy.gunawan@uts.edu.au

Received 17 January 2023; Revised 10 March 2023; Accepted 5 April 2023; Published 25 April 2023

Academic Editor: Jagpreet Singh

The antimicrobial properties of copper are well-known but maintaining a low oxidation state of Cu in particles is difficult. Herein, antimicrobial Cu_xP particles were synthesized through phosphorization of $Cu(OH)_2$, to lock copper in its monovalent state (as Cu_3P). We found that the phosphorization could be achieved at temperatures as low as 200°C, with stable surface presence of Cu(I) on the resulting Cu_xP particles. Cu(I) can act as a one-electron reducing agent for molecular oxygen, to generate the highly reactive hydroxyl radical. In this study, Cu_xP displayed antibacterial activities on the Gram-positive *Staphylococcus aureus* and Gram-negative *Escherichia coli*, with minimum inhibitory concentrations of 32 mg/L for the highest temperature particles (350°C) on both model bacteria. The evident membrane damage is consistent with the intended hydroxyl radical bacterial targeting mechanism. Low-temperature Cu_xP, although exhibiting lower antibacterial efficacies than those of the higher temperature variant, still showed competitive growth inhibiting activities when compared to other reported antimicrobial copper-based particles. The present work showcases advancements in particle technology that can lead to the development of a more robust antimicrobial agent, presenting a potent additive for self-disinfection applications.

1. Introduction

The world is now facing a pandemic-level infection, with pathogens capable of spreading via inanimate objects and surfaces. Research efforts have been increasingly focussed to address this so-called fomite transmission, in particular on the development of self-disinfecting materials. The application of antimicrobial agents on surfaces can reduce the risk of fomite transmission of pathogens in household and hospital settings, with the present work focusing on copper (Cu)-based antimicrobial particles. When compared to other metals, copper-based particles are cheaper to produce, with faster leaching rates, to release the toxic copper ions, including in biological systems [1–3]. Various copper-based antimicrobial particles have been developed, showing both *in vitro* and *in vivo* antibacterial activities [1]. For instance, metallic copper particles have been shown to exhibit bacterial-killing activities, with studies observing the particle apparent physical interactions with bacterial membranes, compromising their integrity [4]. Copper oxide (CuO) particles, on the other hand, have been indicated to exert different antibacterial mechanism, with the so-called Trojan horse-type toxicity. The mechanism involves intracellular leaching of copper ions following particle penetration into cells, leading to cell death and/or growth inhibition [4–7]. Copper-based particles have shown efficacies on Gram-positive and Gram-negative bacteria, both on their free-living planktonic and surface-attached biofilm forms of growth [4–7]. Research inquiries have further described the effects of particle characteristics on their antibacterial activities. Applerot et al. [5] found that smaller CuO particles (~2 nm) were associated with stimulation of a more intense oxidative stress, and therefore, a more effective antibacterial with higher extent of cell killing when compared to the larger particles (~30 nm). Studying the particle shapes, Laha et al. [8]

reported higher cell-killing effects of nanosized spherical CuO on Gram-negative bacteria (*Proteus vulgaris* and *Escherichia coli*), whereas nanosheets of CuO were more effective on Gram-positive bacteria (*Bacillus subtilis* and *Micrococcus luteous*).

Copper has also been combined with other metals to form antimicrobial alloys [9]. Zhou et al. [10] reported the cell-killing activities of Cu_2O–ZrP hybrid nanosheets on methicillin-resistant *Staphylococcus aureus* (MRSA) and vancomycin-resistant *Enterococcus*. The antibacterial effects were shown to correlate with the indicated oxygen radical targeting of bacterial membranes [10]. Likewise, Shalom et al. [7] reported the cell-killing activities of Zn-doped CuO nanoparticles (deposited on catheters) on urinary tract infection-causing bacterial pathogens (*E. coli*, *S. aureus*, and *P. mirabilis*). Combining Cu with silver has shown synergistic antibacterial effects; whereby presence of silver was indicated to increase the bacterial membrane permeability, increasing the growth inhibitory activities of the alloy to up to eight fold (on *E. coli* and *B. subtilis*), when compared to copper alone [11]. Metal ions have been indicated to interact with electronegative groups that are present in membrane phospholipids, with the interactions being linked, at least in part, to increasing membrane permeability and in turn, influx of the ions into bacteria to further disrupt cellular functions, including DNA synthesis [11]. A recent study by Tomina et al. [12] reported a significant increase in the antibacterial (on both Gram-positive and Gram-negative bacteria) and antifungal activities of mono- and bifunctional silica microspheres following doping with Cu(II), which are suggested to correlate with the oxygen radical-generating Fenton-like copper redox cycling (see below), leading to oxidative attack on membranes. Similarly, in a study by Naz et al. [13] Cu(II)-doped O-Carboxymethyl chitosan (OCMC) showed higher antibacterial activity on *E. coli* and *B. subtilis* in comparison to the OCMC alone. Another study by Wilks et al. [14] observed higher cell-killing rates (on *E. coli*) with increasing copper content in alloys with nickel, brass and steel, indicating major antimicrobial contribution from copper.

Copper antimicrobial applications, up to this stage, have explored the use of mainly Cu(II) and Cu(0)-based materials. For instance, quite recent work from our group found that a Cu(II) complex embedded within a poly(vinyl chloride) matrix could effectively inhibit the growth of surface-attached biofilms of nitrifying bacteria. The copper complex system generated nitric oxide, a quorum sensing inhibitor, *via* Cu(II)/Cu(I) redox cycling reactions when in the presence of nitrite and ascorbic acid (note that quorum sensing is a cell-to-cell communication signalling that allow controls of specific biological processes, including biofilm formation and adaptation to external stressors) [15]. Another example is a 3D printed Cu(0)-based self-disinfecting surfaces [16]. For the latter, a study by Champagne and Helfritch [3] demonstrated the cell-killing activities of three copper-based surfaces; developed by the deposition of Cu(0) using plasma spray, wire arc spray, and cold spray; on MRSA [3]. The cold spray technique, which results in the development of copper microstructure morphologies with enhanced diffusion of the toxic copper ions (more specifically, the high-velocity particle impact with the cold spray technique led to high grain dislocations density within the copper deposit, which in turn, increases copper ion diffusion in the metal), displayed the highest antibacterial activities [3]. Another study by Noyce et al. [17] observed a complete killing of MRSA suspensions (10^7 colony forming unit per mL) when exposed for 90 min at 22°C room temperature to Cu(0) surfaces. Although studies have reported the antimicrobial activities of Cu(I)-based materials [1, 2, 18–20], the use of Cu(I) however, is often hindered by its labile nature [15]. Cu(I)-containing antimicrobial systems have rarely been explored without an additional matrix support. Herein, the present work aims to develop a hydroxyl radical-generating antimicrobial copper particles, exploiting the relatively high redox potential of Cu(I). We synthesized Cu(I)-rich Cu_xP particles via facile phosphorization to help stabilize the surface presence of Cu(I) for a redox-based hydroxyl radical generation and studied their antimicrobial effects on model Gram-positive and Gram-negative bacteria. With a lower redox potential, Cu(I) species (Cu(I)/Cu(II) of 0.153 V) is more favorable than Cu(0) species (Cu(0)/Cu(II) of 0.342 V, Cu(0)/Cu(I) of 0.521 V) to induce the one-electron reduction of molecular oxygen (O_2) to form oxygen radicals [19]. The reactions generate superoxide radical $O_2^{\cdot-}$ from O_2 (non-Fenton, reaction 1). The $O_2^{\cdot-}$ then undergoes a proton-coupled electron transfer reaction to form H_2O_2 (Reaction 2), and ultimately, the Fenton-like reaction to form the highly reactive hydroxyl radical (Reaction 3) [21, 22].

Molecular oxygen reduction reactions:

$$O_2 + e^- \longrightarrow O_2^{\cdot-}, \quad (1)$$

$$O_2^{\cdot-} + e^- + 2H^+ \longrightarrow H_2O_2, \quad (2)$$

$$H_2O_2 + e^- \longrightarrow \cdot OH + OH^-. \quad (3)$$

Phosphorization of copper particles allows the locking of Cu in its monovalent state, potentially maintaining a high concentration of Cu(I) on the particle surface [23]. $Cu(OH)_2$ particles were first synthesized (by precipitation from a saturated ammonia solution), followed by phosphorization at different calcination temperatures. The phosphorization process led to the formation of Cu_3P (Cu(I) state) and CuP_2 (Cu(II) state), the latter more prevalent at higher calcination temperatures (≥300°C). Our study found that the Cu_xP particles exhibit competitive growth inhibiting activities when compared to other copper-based particles on the model bacteria. Further, we present studies elucidating the origins of the Cu_xP antibacterial activities, including the hydroxyl radical-mediated targeting.

2. Results

2.1. Synthesis and Characterisation of Cu_xP Particles. Phosphorization of $Cu(OH)_2$ was carried out in the presence of NaH_2PO_2 (under Ar atmosphere, NaH_2PO_2 decomposes to PH_3(g) at ≥200°C) at different calcination temperatures of 150–350°C to obtain CuO150, CuP200, CuP250, CuP300, and CuP350 particles. The extent of phosphorization was

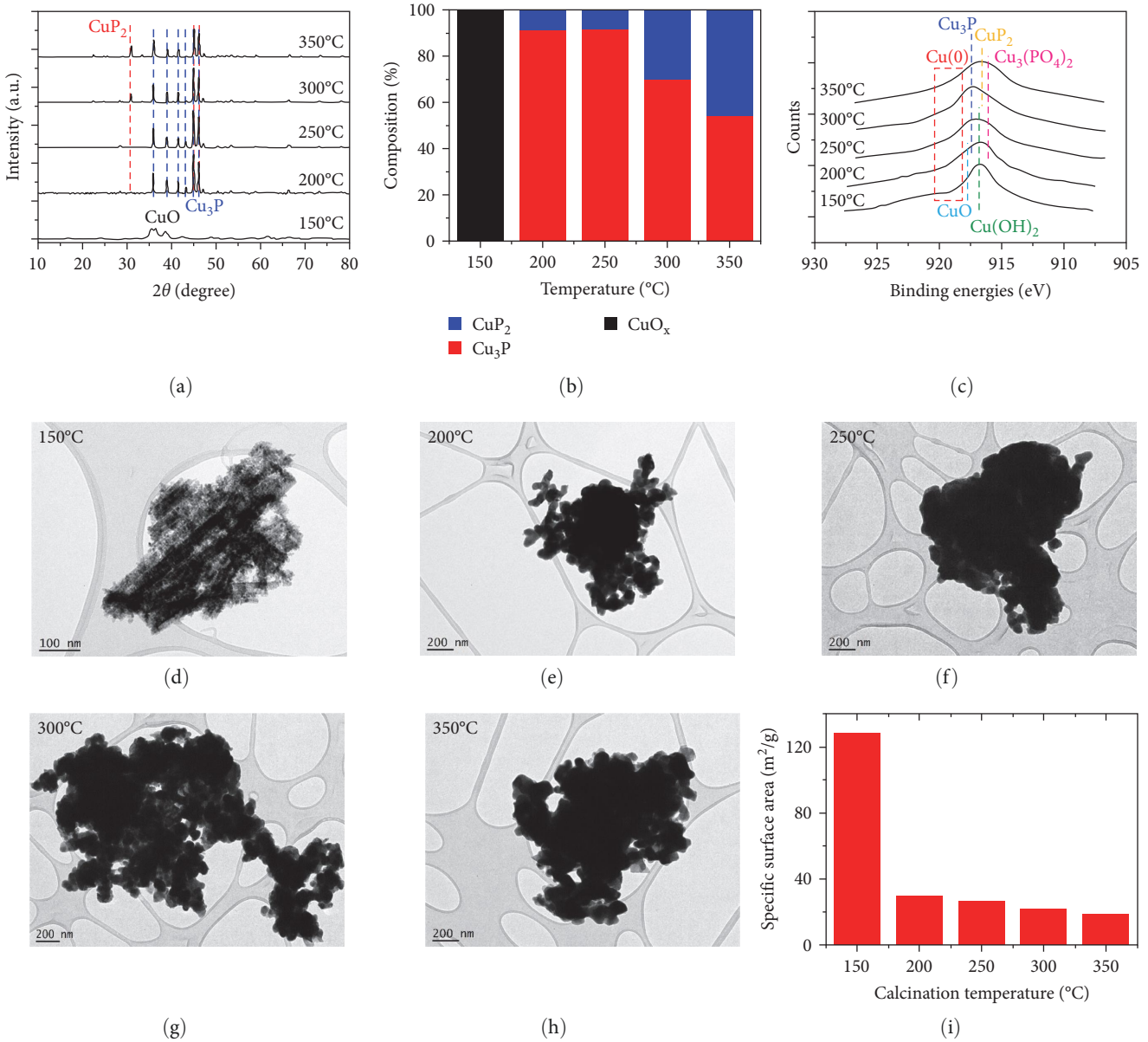

FIGURE 1: Crystal and chemical structure of CuO (150°C) and Cu_xP (200–350°C) particles at different calcination temperatures. (a, b) XRD spectra and bulk phase composition determined from the diffraction contribution of the identified phases, (c) XPS Cu LMM spectra identifying the surface composition, (dh) TEM images, and (i) BET-specific surface area.

examined with X-ray diffraction (XRD, Figure 1(a)). The XRD patterns of the calcined particles showed gradual shifts in chemical composition with increasing temperatures. At 150°C, the samples existed as CuO and Cu_2O, suggesting the dehydration and partial reduction of $Cu(OH)_2$. The oxides formation most likely resulted from direct redox reaction of $Cu(OH)_2$ with NaH_2PO_2, as the calcination temperature (150°C) was not sufficiently high for the NaH_2PO_2-to-PH_3 decomposition. At 200 and 250°C, the CuO and Cu_2O transformed to Cu_3P (Cu(I) state), along with CuP_2, the latter in small amounts (Figure 1(b)). The eutectic formation of CuP_2 became significant at ≥300°C (eutectic formation herein refers to the formation of CuP_2 as part of a solid-solution phase change of Cu_3P/CuP_2 mixture), with 30% of the calcined particles present as CuP_2 at 300°C, and ~45% at 350°C. It is worth noting that the formation of CuP_2 (Cu(II) state) is undesirable as it cannot act as a reducing agent for the intended formation of oxygen radicals.

Using X-ray photoelectron spectroscopy (XPS), we next analyzed the chemical states of Cu of the prepared particles (6 months after synthesis). The particle surface analysis was to also assess for the stable presence of the redox-active Cu(I) species. The Cu LMM spectra of the calcined particles (Figure 1(c)) showed shifts in the binding energies of the peaks with increasing temperatures, corresponding to the complex transitions of $Cu(OH)_2$ to CuO, Cu_3P, and CuP_2 (as well as $Cu_3(PO_4)_2$) (identified according to the work of Biesinger [24]). The presence of Cu LMM peak at 919.2 eV for CuO150

Table 1: Average hydrodynamic sizes, polydispersity index, and zeta potentials of CuO (150°C) and Cu_xP (200–350°C) particles in different media.

Sample	Average size (nm)	Polydispersity index	Zeta potential (mV)[a]
CuO150	114	0.65	–
CuP200	369	0.42	−20.8
CuP250	451	0.49	−27.1
CuP300	341	0.53	−22.0
CuP350	517	0.6	−22.6
PBS[b]	2,158	0.29	–
Tris–HCl[b]	1,197	0.31	−9.6

[a]Zeta potentials were measured in phosphate-buffered saline (PBS at pH 6), [b]CuP300 was dispersed in PBS or tris–HCl for hydrodynamic size, polydispersity index, and zeta potential measurements.

corresponds the surface presence of CuO, whereas the peaks at 917.6 eV for CuP200 to CuP350 calcined particles most likely correspond to the surface presence of the Cu(I) state Cu_3P species (Figure 1(c)). Note that no zero-valent Cu peak was seen in the Cu LMM spectra of the CuP200 to CuP350 particles, which indicates that the occurrence of Cu 2p peaks at 932.8 eV for the particles correspond solely to Cu(I) state (Figure S1). The observations indicate stable Cu(I) surface presence in these particles. For the higher temperature CuP300 and CuP350 calcined particles, the Cu LMM peaks at 916.5 eV most likely correspond to the surface presence of CuP_2 species (Figure 1(c)), which is consistent with the occurrence of the Cu(II) state peaks at 934.7 eV with the Cu 2p spectra (Figure S1). The (surface) detection of Cu_3P and CuP_2 are consistent with the appearance of symmetric P 2p peaks at 129.5 eV and 133.3 eV for the CuP200 to CuP350 particles (Figure S2). Further analysis also showed that a fraction of the (surface) Cu(II) species was present as $Cu_3(PO_4)_2$ for the CuP350 particle, as indicated by the occurrence of asymmetric P 2p peaks at 133.7 eV and 129.8 eV (Figure S2e). Also note that at lower calcination temperatures (≤250°C), some of the (surface) Cu was still present as $Cu(OH)_2$, as indicated by the presence of O 1 s peak at 533.1 eV (Figure S3).

To further understand the phosphorization process, we examined the particle size, morphologies, and aggregation. The electron transmission micrographs of CuO150 (with bulk composition of CuO, Cu_2O as well as $Cu(OH)_2$) showed spherical particles of <10 nm primary size (Figure 1(d)). Following the calcination at higher temperatures (≥200°C), sintering of the particles occurred with significant (~100 nm increments) increase in primary size, with the elevated temperatures, with the particles no longer retaining the spherical morphologies (the sintering was a result of reaction between CuO and $PH_{3(g)}$, the latter was from NaH_2PO_2 decomposition). The measured surface area corroborated with the TEM micrographs of the particles (Figure 1(i)). The specific surface area of CuO150 was determined at 129 m^2/g, and after phosphorization, gradually decreasing to 30 m^2/g with the increasing temperatures (CuP200 to CuP350). The phosphorization, however, only caused minimal change in the particle "overall" aggregate size, with the increasing temperatures. The CuP200 to CuP350 particles (with bulk composition of mainly Cu_3P and CuP_2) fused, forming large aggregates (1,000–2,000 nm, Figure 1(e)–1(h)). Next, the hydrodynamic size of the calcined particles was studied via dynamic light scattering (DLS). As shown in Table 1, the average sizes of the particles are all within ~350–550 nm range (excluding CuO150 with ~100 nm size) when dispersed in water, with polydispersity indexes of 0.40–0.65. Again, we observed no significant impact of the calcination temperature on the hydrodynamic aggregate sizes. The colloidal stability of the CuP300 was further examined in PBS or tris–HCl, the latter used for the antibacterial studies. The average hydrodynamic sizes of CuP300 increased to 2.2 μm and 1.2 μm, respectively, in PBS and tris–HCl, indicating further aggregation and wider size distribution (0.29 (PBS) and 0.31 (tris–HCl) polydispersity index) in the buffer solutions, when compared to the water system. The aggregation was most likely attributed to the presence of relatively high concentrations of anions and counter cations in the buffer solutions, creating a charge shielding effect which neutralises long-range electrostatic interactions, in turn facilitating inter-particle interactions [25]. Smaller CuP300 aggregates were also likely to form in the tris–HCl system (relative to those in the PBS), due to the steric hindrance effects imposed by adsorbed tris molecules [26]. The zeta potential measurement showed a net negative surface charge of the Cu_xP (CuP200 to CuP350) particles in PBS (−20.8 to −27.1 mV). The different calcination temperatures did not seem to affect the zeta potential.

2.2. Oxygen Radical Formation by Cu_xP Particles. The coumarin test was used to assess the hydroxyl radical (·OH) generation of the CuO150 and Cu_xP (CuP200, CuP250, CuP300, CuP350) particles. Coumarin reacts with ·OH to form the fluorescent 7-OH-coumarin (450 nm) [27]. As shown in Figure 2(a), the CuO150 particle did not generate ·OH radicals, with essentially no detection of the fluorescence signal. This is consistent with the XRD and XPS data for CuO150 (Figure 1), showing that the particle is entirely composed of CuO, Cu_2O (and $Cu(OH)_2$), with no surface presence of Cu(I) species. The Cu_xP (Cu_3P and CuP_2) particles CuP200, CuP250, and CuP300 generated ·OH radicals, and at comparable extent, as shown by the overlapping 7-OH-coumarin fluorescence intensity detected over time (Figure 2(a)). The observations are in line with the similar ~50% surface Cu(I) molar ratios (relative to Cu(II)) being estimated for CuP200, CuP250, and CuP300 from the XPS Cu 2p spectra (Figure 2(b), Figure S1). The surface Cu(I) molar ratio decreased to 30% for CuP350. Interestingly, the coumarin

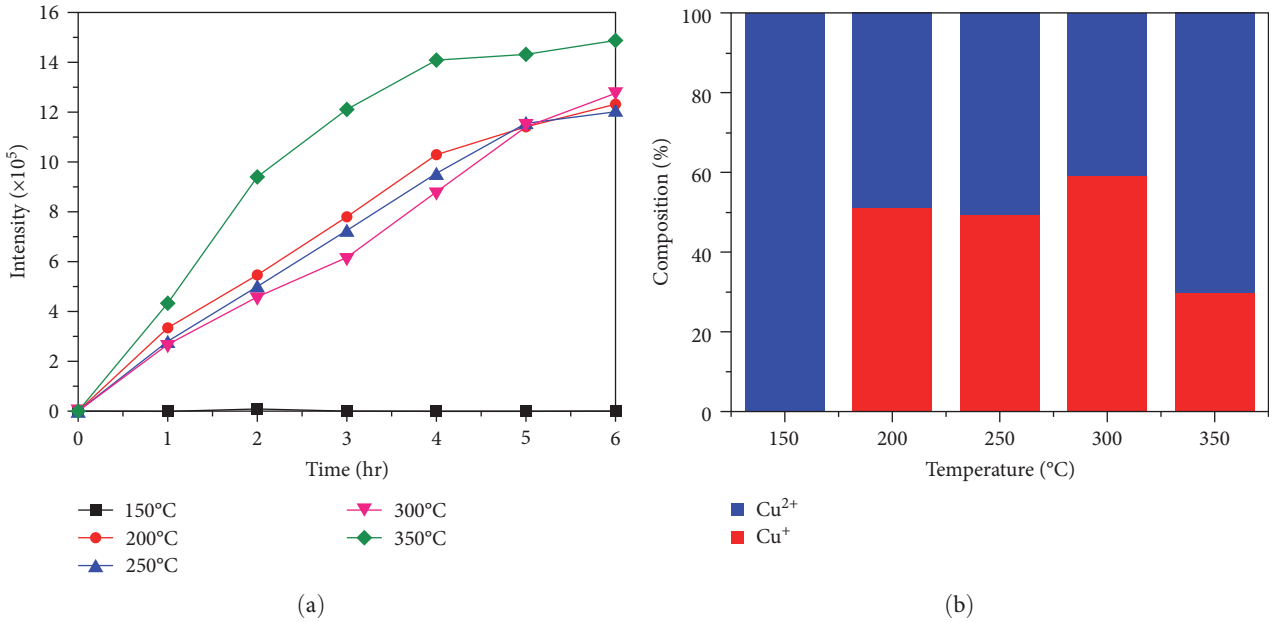

FIGURE 2: (a) Fluorescence signal intensity of 7-OH-coumarin (450 nm) for CuO (150°C) and Cu_xP (200–350°C) particles and (b) surface Cu states molar ratios determined from Cu 2p XPS spectra (Figure S1).

response for CuP350 was apparently the highest when compared to the lower temperature Cu_xP particles, indicating the most extensive ·OH generation. It is still unclear at this stage however, as with the underlying reasons for the highest extent of the radical generation for the CuP350 particles.

2.3. Antibacterial Efficacies of Cu_xP Particles and Mechanistic Studies. The antibacterial effects of the CuO and Cu_xP particles (CuO150, CuP200, 250, 300, 350) were assessed on a Gram-positive model bacterium *S. aureus* and a Gram-negative model bacterium *E. coli*. As shown in Figure 3, all the CuO and Cu_xP particles exhibited dose-dependent toxicity on *S. aureus* and *E. coli*. For example, exposures of *S. aureus* to increasing 8–256 mg/L CuP200 concentrations inhibited the growth of the bacterium, from ~80% extent of biomass growth (relative to the cell-only control growth) at 8 mg/L particle exposure to ~20% growth at 32 mg/L particle concentration, then ultimately to <5% growth at 256 mg/L concentration. Comparable trends were observed with *E. coli*, with ~95% growth at 8 mg/L CuP200 exposure to <5% growth at 256 mg/L particle concentration. Among the particles, CuP350 showed the highest growth inhibition effects with minimum inhibitory concentration (MIC, for ≥95% growth inhibition) of 32 mg/L for both *S. aureus* and *E. coli*, whereas CuO150 showed the lowest effects (MIC of >256 mg/L) (Figure 3). For CuP200, CuP250, and CuP300, the MICs were determined at 64 mg/L for both *S. aureus* and *E. coli*. These CuO and Cu_xP MICs are lower when compared to the previously studied copper-based antibacterial particles, although the much larger sizes of the particles (~100–2000 nm CuO and Cu_xP aggregates, Figure 1(d)1(i), Table 1). Sharma and Kumar [28] reported an MIC of 391 mg/L with CuO particles (d = 5–9 nm) on *E. coli*, whereas Gunawan et al. [29] reported a significantly higher CuO MIC of 900 mg/L (d = 14 nm) on *E. coli*. In another study, Argueta-Figueroa et al. [30] reported a 100 mg/L MIC with metallic Cu^0 particles (d = 4 nm) on *S. aureus* and *E. coli*. The apparent higher extent of growth-inhibiting activity observed in the present study is thought to result, at least in part, from the unique antibacterial mechanisms of the particles, as next described.

The antibacterial activities of our copper particles are most likely to primarily originate from the earlier described redox generation of hydroxyl radical (·OH). The levels of the growth-inhibiting activities are consistent with the extent of the radical generation. CuP350 with the lowest MICs (32 mg/L) on *S. aureus* and *E. coli*, produced the highest amount of ·OH radical, followed by CuP200, CuP250, and CuP300 with less ·OH formation and evidently, higher MICs (64 mg/L) on the bacteria (Figures 2(a) and 3). CuO150 with undetectable ·OH formation seemed to only "reach" MICs for both bacteria at >256 mg/L concentration. Hydroxyl radical is the most reactive oxygen radical, with research inquiries already establishing its reactivity on biomolecules. The one-electron oxidant has been known to cause peroxidation of phospholipids in bacterial cell envelopes (present in the inner membrane of *S. aureus*, and in the outer and inner membranes of *E. coli*) [31]. Initiated by abstraction of an allylic hydrogen atom, the peroxidation modifies lipids into lipid hydroperoxides. The radical can also cleave phosphate esters in phospholipids [31, 32]. These radical attacks on phospholipids, in many cases, have been known to result in leaky membranes [33, 34]. Herein, we stained the particle-exposed *E. coli* samples with AM1-43 fluorescent dye to probe the cell membranes phospholipid moieties [35, 36]. Indeed, leaky membranes were observed in the *E. coli* population for all tested particles (Figure 4). Note the less fluorescent (green) membranes of the particle-exposed bacterial samples when

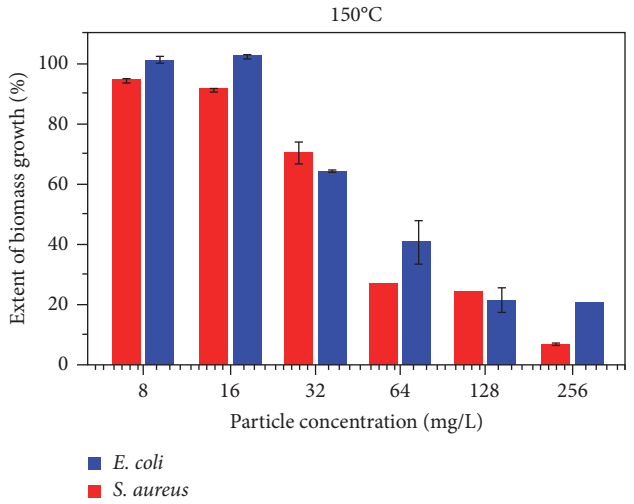

(a)

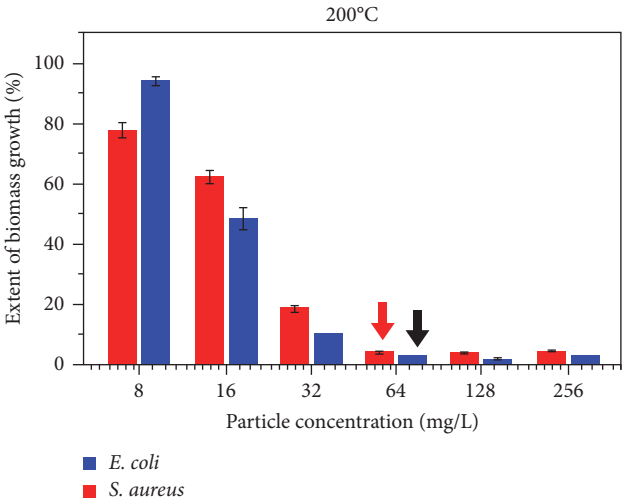

(b)

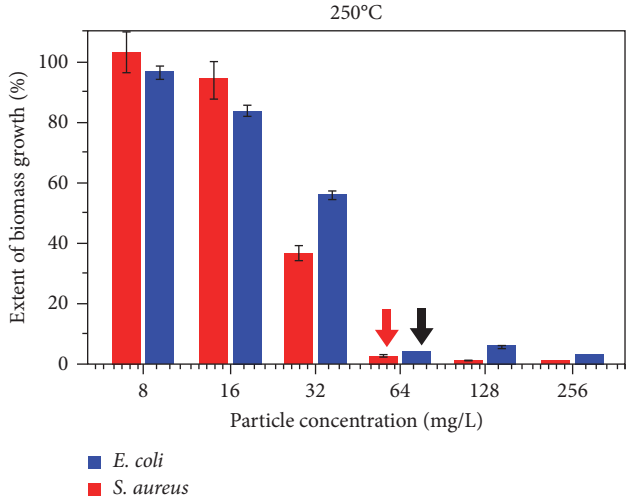

(c)

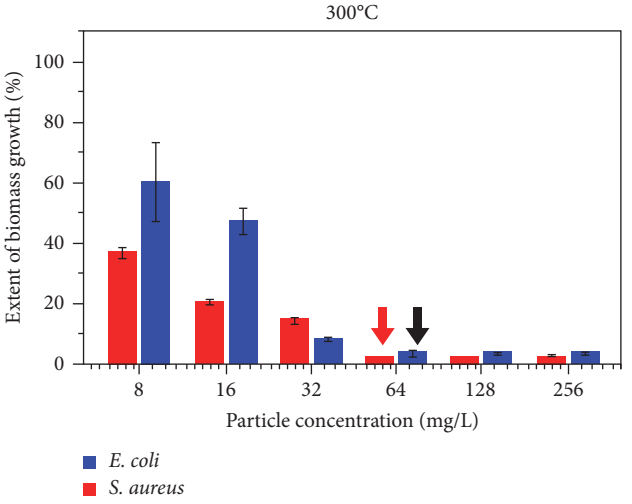

(d)

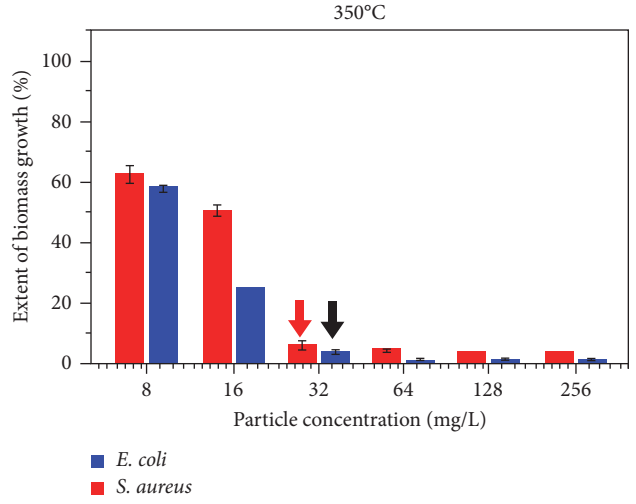

(e)

Temperature (°C)	MIC (mg/L)	
	EC	SA
150	-	-
200	64	64
250	64	64
300	64	64
350	32	32

(f)

Figure 3: Antimicrobial activities of CuO (150°C) and Cu_xP (200–350°C) particles on model bacteria. (a–e) exposure of Gram-positive (*S. aureus*) and Gram-negative (*E. coli*) bacteria to 8–256 mg/L particles at 37°C, 16 hr. The extent of biomass growth was determined relative to cell-only (no particles) control samples. For each of the particle concentration, the experiments were performed with three biological replicates (independent bacterial inocula), each with three technical replicates. (f) The minimum inhibitory concentrations (correspond to ≤5% growth relative to the cell-only control samples) for each of the particle exposure systems.

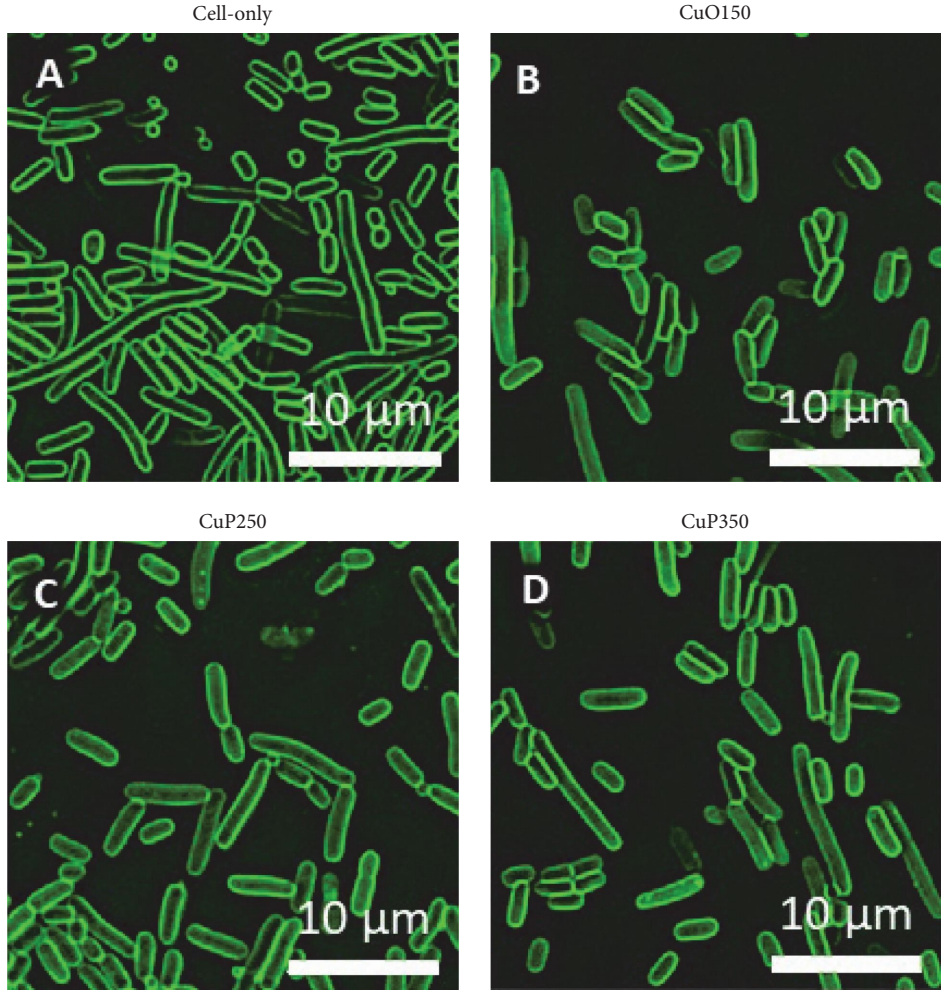

Figure 4: Fluorescence micrographs of AM1-43 stained *E. coli* following exposures to CuO and Cu_xP particles. Also shown is the cell-only (no particle) control. The bacteria were exposed to 64 mg/L particle concentration for 1 hr.

compared to the cell-only control. The leaky membrane is also indicated by an influx of the dye into cells, with the evident green fluorescence mass inside the particle-exposed samples, which is absent in the cell-only control [37, 38].

The phospholipid fluorescence staining was also performed on the particle-exposed *S. aureus* samples, however, with inconclusive results (Figure S4). This rather expected observation is likely to result from the presence of relatively thick, outermost peptidoglycan layer in the Gram-positive cell envelope, hence limiting the dye penetrability to reach the inner membrane. Regardless, earlier nanoparticle studies have shown that peptidoglycan is also prone to hydroxyl radical attack [31]. The radical can damage amide bonds that are present in the glycan strands (more specifically, in the amino sugars and peptide moieties) of peptidoglycan. Studies have also indicated hydroxyl radical attack on teichoic acid, another major cell envelope component of Gram-positive bacteria; with the radical targeting the C=O ester, phosphate ester, and amide bonds in the molecule [31]. The known hydroxyl radical targeting on Gram-positive cell envelope components could explain the similar antibacterial activities herein observed between the Gram-positive and Gram-negative models. Taken together, the indicative observations of hydroxyl-radical mediated cell envelope damages, shown with membrane phospholipids in the present work, are in agreement with the growth-inhibiting effects of the CuP350, along with the less potent CuP200, CuP250, and CuP300 particles. The radical is also known to target base pairing in DNA and RNA, as well as introducing covalent modifications in amino acids, such as the sulfur-containing cysteine and methionine, in turn inactivating functional proteins [39–43].

A more detailed investigation revealed other sources for the antibacterial activities, apart from the redox hydroxyl radical generation. This is particularly apparent with the dose-dependent growth inhibition effects seen with the non-hydroxyl radical-producing CuO150 particle (Figure 3(a)). Our leaching studies found that the particle almost completely dissolved (~80% relative to total copper content, measured in MHB culture medium, pH 6), releasing soluble copper into

the exposure systems (Figure S5). The CuO150 is composed of Cu_xO with mainly CuO on its surface (Figure 1). Studies have reported relatively high extent of soluble copper leaching from CuO particles in organic-containing media due to complexation-mediated leaching [29]. Previous work on copper-based particles have established the antibacterial roles of the leached soluble copper, which stimulate oxidative stress in cells, being linked to Cu(II) ion targeting of proteins [29, 43]. A borderline Lewis acid, the ion has high affinities to donor groups in amino acid side chains, such as the $–NH^+$ (in imidazole ring), $–NH_3^+$, and thiol ($–S^-$) groups in histidine, lysine, and cysteine, respectively, forming complexes with the amino acids in proteins [44]. The ion can also disrupt the iron–sulfur (cysteine) clusters that are present in many physiologically essential biosynthetic and catabolic enzymes, releasing the Fenton-active Fe(II) ion, with the latter further reacting with cellular H_2O_2 to form hydroxyl radical [45]. Cu(II) ion has also been indicated to target cell envelopes, disrupting functional groups in peptidoglycan (peptidoglycan is also present in Gram-negative bacteria, as thin layer in between the outer and inner membranes) and phospholipids, the latter affecting membrane permeability [46, 47]. The implied leached soluble Cu-mediated cellular hydroxyl radical generation and cell envelope targeting are consistent with the damaged membrane observation, herein also evident with the CuO150-exposed bacterial samples (Figure 4(b)).

The soluble copper leaching could also contribute to the growth-inhibiting effects of the higher temperature Cu_xP particles. The CuP350 (composed of ∼55% Cu_3P and ∼45% CuP_2, with surface presence of Cu_3P, CuP_2, and $Cu_3(PO_4)_2$, Figure 1) and CuP250 (∼90% Cu_3P and ∼10% CuP_2, with surface presence of mainly Cu_3P and $Cu(OH)_2$, Figure 1) particles had similar extent of soluble copper leaching (∼7% relative to total copper, Figure S5), although much less when compared to CuO150 (∼80% leaching relative to total copper). In addition to the different particle surface composition, the lower leaching could result from the larger aggregate size of the higher temperature Cu_xP particles (Table 1) [5]. Finally, the data also suggest a potential antibacterial contribution from the solid particulates that remain after leaching. This is evident with the CuP300 bacterial exposures, with already ∼40%–60% growth inhibition effects manifesting on both *S. aureus* and *E. coli* at the lowest particle dosage (8 mg/L, Figure 3(d)), despite the only moderate redox hydroxyl radical generation (Figure 2(a)) and leaching of soluble copper (Figure S5). Research inquiries have reported that copper particles can adhere onto bacterial membranes through electrostatic interaction, which leads to membrane damage and in some case, penetration of the particles into the cytoplasm [48–50].

3. Conclusion

Herein, we developed Cu_xP particles for antibacterial purposes, with stable surface presence of Cu(I) species intended for the redox generation of the highly reactive hydroxyl radical. The particles were synthesized via a temperature-dependent phosphorization of $Cu(OH)_2$, with particle surface analysis confirming the stable presence of the Cu(I) state Cu_3P species. The phosphorization process, however, led to sintering effects and increased the particle size. Despite the larger particle size, our studies with Gram-positive and Gram-negative bacteria models showed a significantly higher extent of antimicrobial activities when compared to other copper-based particles. The Cu_xP particles were found to generate hydroxyl radical, most likely involving one-electron reduction of molecular oxygen by the surface Cu(I), leading to the observed inhibition effects on bacterial growth, with further evidence of cell membrane targeting. In summary, the Cu_xP particles with their ability to use molecular oxygen to generate radicals, as well as, apparently, their relatively low extent of copper leaching, present a promising particle technology for alternative antimicrobial applications, in particular for the development of self-disinfecting surfaces, to slow down the fomite transmission of pathogens.

Data Availability

The data used to support the findings of this study are included within the article and supplementary information file.

Conflicts of Interest

The authors declare that they have no conflicts of interest.

Funding

Open access publishing facilitated by University of Technology Sydney, as part of the Wiley - University of Technology Sydney agreement via the Council of Australian University Librarians.

Acknowledgments

The work was supported by the Australian Research Council Discovery Project DP200103587 (Z. Gu) and DP180100474 (C. Gunawan). The authors would also like to acknowledge the use of the facilities within the UNSW Mark Wainwright Analytical Centre and the UoW Electron Microscopy Centre.

Supplementary Materials

Figure S1: Cu 2p XPS spectra of (a) CuO150 and phosphorized Cu_xP: (b) CuP200, (c) CuP250, (d) CuP300, and (e) CuP350. Figure S2: P 2p XPS spectra of (a) CuO150 and phosphorized Cu_xP: (b) CuP200, (c) CuP250, (d) CuP300, and, (e) CuP350. Figure S3: O 1s XPS spectra of (a) CuO150 and phosphorized Cu_xP: (b) CuP200, (c) CuP250, (d) CuP300, and (e) CuP350. Figure S4: Fluorescence micrographs of fluorescent dye (FM4-64) stained *S. aureus* after exposure to Cu_xP particles: (a) Blank, (b) CuO150, (c) CuP250, and (d) CuP350. Figure S5: Solubility of CuO and Cu_xP particles in (a) MHB buffer solution at pH 6 and (b) deionized water. (*Supplementary Materials*)

References

[1] M. L. Ermini and V. Voliani, "Antimicrobial nano-agents: the copper age," *ACS Nano*, vol. 15, no. 4, pp. 6008–6029, 2021.

[2] I. Salah, I. P. Parkin, and E. Allan, "Copper as an antimicrobial agent: recent advances," *RSC Advances*, vol. 11, pp. 18179–18186, 2021.

[3] V. K. Champagne and D. J. Helfritch, "A demonstration of the antimicrobial effectiveness of various copper surfaces," *Journal of Biological Engineering*, vol. 7, Article ID 8, 2013.

[4] H. L. Karlsson, P. Cronholm, Y. Hedberg et al., "Cell membrane damage and protein interaction induced by copper containing nanoparticles—importance of the metal release process," *Toxicology*, vol. 313, no. 1, pp. 59–69, 2013.

[5] G. Applerot, J. Lellouche, A. Lipovsky et al., "Understanding the antibacterial mechanism of CuO nanoparticles: revealing the route of induced oxidative stress," *Small*, vol. 8, no. 21, pp. 3326–3337, 2012.

[6] Z. Wang, N. Li, J. Zhao, J. C. White, P. Qu, and B. Xing, "CuO nanoparticle interaction with human epithelial cells: cellular uptake, location, export, and genotoxicity," *Chemical Research in Toxicology*, vol. 25, no. 7, pp. 1512–1521, 2012.

[7] Y. Shalom, I. Perelshtein, N. Perkas, A. Gedanken, and E. Banin, "Catheters coated with Zn-Doped CuO nanoparticles delay the onset of catheter-associated urinary tract infections," *Nano Research*, vol. 10, pp. 520–533, 2017.

[8] D. Laha, A. Pramanik, A. Laskar, M. Jana, P. Pramanik, and P. Karmakar, "Shape-dependent bactericidal activity of copper oxide nanoparticle mediated by DNA and membrane damage," *Materials Research Bulletin*, vol. 59, pp. 185–191, 2014.

[9] A. Różańska, A. Chmielarczyk, D. Romaniszyn et al., "Antimicrobial properties of selected copper alloys on staphylococcus aureus and *Escherichia coli* in different simulations of environmental conditions: with vs. without organic contamination," *International Journal of Environmental Research and Public Health*, vol. 14, no. 7, Article ID 813, 2017.

[10] J. Zhou, H. Xiang, F. Zabihi, S. Yu, B. Sun, and M. Zhu, "Intriguing antisuperbug Cu_2O@ZrP hybrid nanosheet with enhanced antibacterial performance and weak cytotoxicity," *Nano Research*, vol. 12, pp. 1453–1460, 2019.

[11] J. A. Garza-Cervantes, A. Chávez-Reyes, E. C. Castillo et al., "Synergistic antimicrobial effects of silver/transition-metal combinatorial treatments," *Scientific Reports*, vol. 7, Article ID 903, 2017.

[12] V. V. Tomina, I. M. Furtat, A. P. Lebed et al., "Diverse pathway to obtain antibacterial and antifungal agents based on silica particles functionalized by amino and phenyl groups with Cu(II) ion complexes," *ACS Omega*, vol. 5, no. 25, pp. 15290–15300, 2020.

[13] A. Naz, S. Arun, S. S. Narvi et al., "Cu(II)-carboxymethyl chitosan-silane schiff base complex grafted on nano silica: structural evolution, antibacterial performance and dye degradation ability," *International Journal of Biological Macromolecules*, vol. 110, pp. 215–226, 2018.

[14] S. A. Wilks, H. Michels, and C. W. Keevil, "The survival of *Escherichia coli* O157 on a range of metal surfaces," *International Journal of Food Microbiology*, vol. 105, no. 3, pp. 445–454, 2005.

[15] V. Wonoputri, C. Gunawan, S. Liu et al., "Copper complex in poly(vinyl chloride) as a nitric oxide-generating catalyst for the control of nitrifying bacterial biofilms," *ACS Applied Materials & Interfaces*, vol. 7, no. 40, pp. 22148–22156, 2015.

[16] T. Q. Tran, A. Chinnappan, J. K. Y. Lee et al., "3D printing of highly pure copper," *Metals*, vol. 9, no. 7, Article ID 756, 2019.

[17] J. O. Noyce, H. Michels, and C. W. Keevil, "Potential use of copper surfaces to reduce survival of epidemic meticillin-resistant staphylococcus aureus in the healthcare environment," *Journal of Hospital Infection*, vol. 63, no. 3, pp. 289–297, 2006.

[18] Y. Fujimori, T. Sato, T. Hayata et al., "Novel antiviral characteristics of nanosized copper(I) iodide particles showing inactivation activity against 2009 pandemic H1N1 influenza virus," *Applied and Environmental Microbiology*, vol. 78, no. 4, pp. 951–955, 2012.

[19] N. Shionoiri, T. Sato, Y. Fujimori et al., "Investigation of the antiviral properties of copper iodide nanoparticles against feline calicivirus," *Journal of Bioscience and Bioengineering*, vol. 113, no. 5, pp. 580–586, 2012.

[20] W. Wang, B. Li, H. Yang et al., "Efficient elimination of multidrug-resistant bacteria using copper sulfide nanozymes anchored to graphene oxide nanosheets," *Nano Research*, vol. 13, pp. 2156–2164, 2020.

[21] S. Hussain, E. Aneggi, and D. Goi, "Catalytic activity of metals in heterogeneous fenton-like oxidation of wastewater contaminants: a review," *Environmental Chemistry Letters*, vol. 19, pp. 2405–2424, 2021.

[22] A. V. Kachur, K. D. Held, C. J. Koch, and J. E. Biaglow, "Mechanism of production of hydroxyl radicals in the copper-catalyzed oxidation of dithiothreitol," *Radiation Research*, vol. 147, no. 4, pp. 409–415, 1997.

[23] D. Chao, Q. Dong, J. Chen et al., "Highly efficient disinfection based on multiple enzyme-like activities of Cu_3P nanoparticles: a catalytic approach to impede antibiotic resistance," *Applied Catalysis B: Environmental*, vol. 304, Article ID 121017, 2022.

[24] M. C. Biesinger, "Advanced analysis of copper X-ray photoelectron spectra," *Surface and Interface Analysis*, vol. 49, no. 13, pp. 1325–1334, 2017.

[25] K. Afshinnia and M. Baalousha, "Effect of phosphate buffer on aggregation kinetics of citrate-coated silver nanoparticles induced by monovalent and divalent electrolytes," *Science of The Total Environment*, vol. 581-582, pp. 268–276, 2017.

[26] N. F. D. Vecchia, A. Luchini, A. Napolitano et al., "Tris buffer modulates polydopamine growth, aggregation, and paramagnetic properties," *Langmuir*, vol. 30, no. 32, pp. 9811–9818, 2014.

[27] V. Leandri, J. M. Gardner, and M. Jonsson, "Coumarin as a quantitative probe for hydroxyl radical formation in heterogeneous photocatalysis," *The Journal of Physical Chemistry C*, vol. 123, no. 11, pp. 6667–6674, 2019.

[28] S. Sharma and K. Kumar, "Aloe-vera leaf extract as a green agent for the synthesis of CuO nanoparticles inactivating bacterial pathogens and dye," *Journal of Dispersion Science and Technology*, vol. 42, no. 13, pp. 1950–1962, 2021.

[29] C. Gunawan, W. Y. Teoh, C. P. Marquis, and R. Amal, "Cytotoxic origin of copper(II) oxide nanoparticles: comparative studies with micron-sized particles, leachate, and metal salts," *ACS Nano*, vol. 5, no. 9, pp. 7214–7225, 2011.

[30] L. Argueta-Figueroa, R. A. Morales-Luckie, R. J. Scougall-Vilchis, and O. F. Olea-Mejía, "Synthesis, characterization and antibacterial activity of copper, nickel and bimetallic Cu–Ni nanoparticles for potential use in dental materials," *Progress in Natural Science: Materials International*, vol. 24, no. 4, pp. 321–328, 2014.

[31] C. Gunawan, M. B. Faiz, R. Mann et al., "Nanosilver targets the bacterial cell envelope: the link with generation of reactive oxygen radicals," *ACS Applied Materials & Interfaces*, vol. 12, no. 5, pp. 5557–5568, 2020.

[32] A. Samunl and P. Neta, "Electron spin resonance study of the reaction of hydroxyl radicals with pyrrole, imidazole, and related compounds," *The Journal of Physical Chemistry*, vol. 77, no. 13, pp. 1629–1635, 1973.

[33] H. Yin, L. Xu, and N. A. Porter, "Free radical lipid peroxidation: mechanisms and analysis," *Chemical Reviews*, vol. 111, no. 10, pp. 5944–5972, 2011.

[34] R. Hong, T. Y. Kang, C. A. Michels, and N. Gadura, "Membrane lipid peroxidation in copper alloy-mediated contact killing of *Escherichia coli*," *Applied and Environmental Microbiology*, vol. 78, no. 6, pp. 1776–1784, 2012.

[35] I. Fishov and C. L. Woldringh, "Visualization of membrane domains in *Escherichia coli*," *Molecular Microbiology*, vol. 32, no. 6, pp. 1166–1172, 1999.

[36] J. R. Zupan, T. A. Cameron, J. Anderson-Furgeson, and P. C. Zambryski, "Dynamic FtsA and FtsZ localization and outer membrane alterations during polar growth and cell division in *Agrobacterium tumefaciens*," *Proceedings of the National Academy of Sciences*, vol. 110, no. 22, pp. 9060–9065, 2013.

[37] L. R. Griffing, "FRET analysis of transmembrane flipping of FM4–64 in plant cells: is FM4–64 a robust marker for endocytosis?" *Journal of Microscopy*, vol. 231, no. 2, pp. 291–298, 2008.

[38] J. Derk Te Winkel, D. A. Gray, K. H. Seistrup, L. W. Hamoen, and H. Strahl, "Analysis of antimicrobial-triggered membrane depolarization using voltage sensitive dyes," *Frontiers in Cell and Developmental Biology*, vol. 4, Article ID 29, 2016.

[39] S. B. Nimse and D. Pal, "Free radicals, natural antioxidants, and their reaction mechanisms," *RSC Advances*, vol. 5, pp. 27986–28006, 2015.

[40] M. A. Kohanski, D. J. Dwyer, B. Hayete, C. A. Lawrence, and J. J. Collins, "A common mechanism of cellular death induced by bactericidal antibiotics," *Cell*, vol. 130, no. 5, pp. 797–810, 2007.

[41] B. Ezraty, A. Gennaris, F. Barras, and J.-F. Collet, "Oxidative stress, protein damage and repair in bacteria," *Nature Reviews Microbiology*, vol. 15, pp. 385–396, 2017.

[42] B. D'Autréaux and M. B. Toledano, "ROS as signalling molecules: mechanisms that generate specificity in ROS homeostasis," *Nature Reviews Molecular Cell Biology*, vol. 8, pp. 813–824, 2007.

[43] G. Guan, L. Zhang, J. Zhu, H. Wu, W. Li, and Q. Sun, "Antibacterial properties and mechanism of biopolymer-based films functionalized by CuO/ZnO nanoparticles against *Escherichia coli* and *Staphylococcus aureus*," *Journal of Hazardous Materials*, vol. 402, Article ID 123542, 2021.

[44] R. Osterberg and B. Sjoberg, "Copper(I) and Copper(II) complexes in solution and the crystalline state," *Journal of The American Oil Chemists Society*, vol. 48, no. 10, pp. 525-526, 1971.

[45] E. Valentin, A. L. Bottomley, G. S. Chilambi et al., "Heritable nanosilver resistance in priority pathogen: a unique genetic adaptation and comparison with ionic silver and antibiotics," *Nanoscale*, vol. 12, pp. 2384–2392, 2020.

[46] T. Ishida, "Bacteriolyses of bacterial cell walls by Cu(II) and Zn(II) ions based on antibacterial results of dilution medium method and halo antibacterial test," *Journal of Advanced Research in Biotechnology*, vol. 2, no. 2, pp. 1–12, 2017.

[47] Z. Liu, J. Ye, A. Rauf et al., "A flexible fibrous membrane based on copper(ii) metal–organic framework/poly(lactic acid) composites with superior antibacterial performance," *Biomaterials Science*, vol. 9, pp. 3851–3859, 2021.

[48] A. Thill, O. Zeyons, O. Spalla et al., "Cytotoxicity of CeO_2 nanoparticles for *Escherichia coli*. physico-chemical insight of the cytotoxicity mechanism," *Environmental Science & Technology*, vol. 40, no. 19, pp. 6151–6156, 2006.

[49] J. S. McQuillan, H. G. Infante, E. Stokes, and A. M. Shaw, "Silver nanoparticle enhanced silver ion stress response in *Escherichia coli* K12," *Nanotoxicology*, vol. 6, no. 8, pp. 857–866, 2012.

[50] Y.-N. Chang, M. Zhang, L. Xia, J. Zhang, and G. Xing, "The toxic effects and mechanisms of CuO and ZnO nanoparticles," *Materials*, vol. 5, no. 12, pp. 2850–2871, 2012.